MEASUREMENT OF UNSTEADY CHARACTERISTICS OF ENDWALL VORTICES USING SURFACE-MOUNTED HOT-FILM SENSORS

A thesis submitted in partial fulfillment of the requirements for the degree of

Master of Science in Mechanical Engineering

By

EMMA MICHELLE VELEY

B.S.M.E., Wright State University, 2017

2018

Wright State University

WRIGHT STATE UNIVERSITY

GRADUATE SCHOOL

May 8th, 2018

I HEREBY RECOMMEND THAT THE THESIS PREPARED UNDERY MY SUPERVISION BY Emma Michelle Veley ENTITLED Measurement of Unsteady Characteristics of Endwall Vortices Using Surface-Mounted Hot-Film Sensors BE ACCEPTED IN PARTIAL FULFILLMENT OF THE REQUIREMENTS FOR THE DEGREE OF Master of Science in Mechanical Engineering.

Committee on Final Examination

Mitch Wolff, Ph.D.

Rolf Sondergaard, Ph.D., PE

Christopher Marks, Ph.D.

Barry Milligan, Ph.D.
Interim Dean of the Graduate School

Mitch Wolff, Ph.D.
Thesis Advisor

Dr. Joseph Slater
Chair, Department of Mechanical and Materials Engineering

ABSTRACT

Veley, Emma Michelle, M.S.M.E. Department of Mechanical and Materials Engineering, Wright State University, 2018. Measurement of Unsteady Characteristics of Endwall Vortices Using Surface-Mounted Hot-Film Sensors

High-lift low-pressure turbine blades produce significant losses at the junction with the endwall. The losses are caused by several complex three-dimensional vortical flow structures, which interact with the blade suction surface boundary layer. This study investigates the unsteady characteristics of these endwall flow structures on a highly loaded research profile and the adjacent endwall using surface-mounted hot-film sensors. Experiments were conducted in a low-speed linear cascade wind tunnel. The front-loaded blade profile was subjected to three different inlet conditions, consisting of two turbulence levels, and three incoming boundary layer thicknesses. Multiple surface-mounted hot-film sensors were installed throughout the passage.

This thesis progressed in three stages of research. The first verified that the hot-film sensors could be used to detect flow structures in the cascade. The second used the results from installed hot-films to examine the unsteady characteristics of vortices formed near the leading edge and the propagation of the passage vortex across the passage where it interacts with a corner separation along the suction surface. Simultaneous measurements from the hot-film sensors were analyzed for frequency spectra and time lag in order to provide new insight into the endwall flow dynamics. Finally, signatures from the hot-films were linked to specific flow phenomena through concurrent flow visualization. At each stage of the investigation, results were compared to the results of a numerical simulation.

Table of Contents

List of Figures

List of Tables

Acknowledgments

I'd like to thank Jacob Dickel for teaching me that if you want something done right, do it yourself. I'd like to thank Nathan Fletcher for teaching me that if you want something done fast, do it yourself. I'd like to thank Chris Marks for teaching me that if you want to fry something, do it yourself. Thank you, Dr. Chris Marks, for all your wisdom about low pressure turbine endwall flow, Roth IRAs, astronomy, ukuleles, pinewood derby cars, etc., and for your ability to pester for a laser permit. I would like to thank Philip Bear for the initial lab and grad school advice when I started in the LSWT facility.

I would like to thank the Air Force Research Labs and the Pathways Internship program for employing me and letting me use the facilities to complete my work.

I would like to thank Gerry Landis for donning the task of hot-film production, allowing me to contend with the IFA 300 without letting defenestration of the system become a reality.

I would like to thank Drs. Rolf Sondergaard and Rich Anthony for their wondrous tid-bits of knowledge and advice, even if I ignored the advice to start writing sooner. I would also like to thank Dr. Sondergaard for the amazing organization of the toolboxes, which increased my ability to find allen wrenches. I would also like to thank Dr. Andreas Gross for his ILES wizardry.

I would like to thank Dr. Wolff for being a great professor with a good sense of humor to withstand all the rascally comments from us snarky grad students, and for his willingness to go above and beyond when dealing with bureaucracy.

I would like to thank Wendy's and anywhere that makes cheddar broccoli soup for fueling the researcher.

I would also like to thank my family and my church family for their support and welcome distractions during this time. And lastly I would like to thank God for giving these opportunities… and for duct tape.

Nomenclature

AFRL	Air Force Research Laboratory
C_x	Chord, [cm]
CCA	Constant Current Anemometer
c_f	Skin-Friction Coefficient
CTA	Constant Temperature Anemometer
d	Diameter, [m]
E	Voltage, [V]
f	Frequency, [Hz]
FFT	Fast Fourier Transform
FSTI	Freestream Turbulence Intensity
H	Span
$\mathscr{H}$	Shape Factor
HV	Horseshoe Vortex
ILES	Implicit Large Eddy Simulation
GTE	Gas Turbine Engine
k	Thermal Conductivity of Fluid
LPT	Low Pressure Turbine
LSWT	Low Speed Wind Tunnel
Nu	Nusselt Number
P	Pressure, [Pa]
Pr	Prandtl Number

PS	Pressure Side/Surface
PV	Passage Vortex
q	Dynamic Pressure, $\frac{1}{2}\rho U^2$
Q	Q-Criterion, $Q = \frac{1}{2}\left[\left\{\frac{1}{2}\left(\frac{\partial U_i}{\partial x_j} - \frac{\partial U_j}{\partial x_i}\right)\right\}^2 - \left\{\frac{1}{2}\left(\frac{\partial U_i}{\partial x_j} + \frac{\partial U_j}{\partial x_i}\right)\right\}^2\right]$
R	Normalized Correlation Coefficient
Re	Reynolds Number
SS	Suction Side/Surface
SPIV	Stereographic Particle Image Velocimetry
St	Strouhal Number, $\frac{fd}{U}$
T	Temperature [K]
TPR	Temperature Power Ratio
U,u	Velocity [m/s]
$\overline{U}$	Mean Velocity [m/s]

Greek

γ_t	Total Pressure Loss Coefficient, $\frac{P_{t,in} - P_{t,out}}{\frac{1}{2}\rho U_{in,st}^2}$
$\delta_{99\%}$	Boundary Layer Thickness
δ^*	Displacement Thickness
θ	Momentum Thickness
λ	Wavelength
ν	Kinematic Viscosity, 1.5 x 10^{-5} m^2/s
ρ	Density, [kg/m^3]
τ	Time lag
τ_q	Quasi-Shear Stress

Subscripts

a	Ambient
C_x	Axial Chord
d	Diameter
in	Inlet Condition
out	Outlet Condition
PS	Passage
s	Static
t	Total
w	Across Sensor
x	Axial
0	Under Zero Flow
2D	Midspan
∞	Freestream

Superscripts

*	Dimensionless Quantity

1. Introduction

1.1 Motivation

A goal of research related to the Low Pressure Turbine (LPT) in a Gas Turbine Engine (GTE) is to decrease weight and cost. The easiest and most feasible execution of this goal is to decrease the number of blades in the LPT. With a decrease in blade count, the pitch spacing increases and consequently, with fixed gas angles, an increase in loading per blade occurs. However, high-lift blades have greater losses from the junction flow, due to the greater impact of pressure gradients that increase the boundary layer separation, which strengthens the secondary flow field vortical structures.

The secondary flows in the endwall region are estimated to make up from one-third to one-half of the loss through a row of high-lift turbine blades [Denton 1993, Harrison 1990]. Due to the high losses incurred by the secondary flow, both passive and active methods of loss reduction have been studied. Passive flow control includes blade and endwall contouring [Bear 2016, Marks et al. 2016, Dickel et al. 2018]; active flow control includes steady/unsteady blowing and plasma actuators [Benton et al. 2013, Marks 2011]. Unsteady active methods are used to excite natural instabilities of the passage flow structures. An understanding of these instabilities is key to implementing these methods.

Prior research has shown that front loading a high-lift profile can result in a gradual pressure recovery over the suction surface [McQuilling 2007]. The smaller adverse pressure gradient makes the profile more resistant to separation at low Reynolds numbers. While excellent midspan performance has been demonstrated with front-loaded high-lift blade profiles, additional research is required to better understand loss generation in the endwall region caused by secondary

flows. Knowledge of endwall flow dynamics will lead to better computational design methods and techniques to mitigate losses in the endwall region.

The goal of this thesis is to use surface-mounted constant-temperature hot-film sensors to measure fluctuations in the flow caused by near wall flow features at the junction of a blade and endwall. More specifically, the goal is to relate characteristic signatures of the hot-film signal to flow structures away from the wall.

A front-loaded high-lift LPT research profile, the L2F, is used in the study. Measurements are taken in a low-speed wind tunnel with no bulk temperature gradient. The hot-films are mounted on the endwall and blade suction surfaces and operated in a constant temperature mode using the bridge, amplifier, and signal conditioning from a commercial multi-channel thermal anemometry system.

Similar sensors have been used to measure shear stress, as shown by Bellhouse et al. [1966], or quasi-shear stress with an uncalibrated hot-films as described by Hodson [1984]. Others have used such methods to look at the turbulence on the suction surface and the separation bubble of airfoils and LPT blades [Zhang et al. 2002, Nakayama et al. 1993, Stack et al. 1987]. Stack et al. provides an overview of what each type of raw signal under different flow regimes – laminar, transitional, turbulent, and separated – should look like [1987]. Similarly, the boundary layer on the endwall of an LPT has been analyzed using hot-films [Vera et al. 2009]. The analyses of the suction surface show that the hot-film sensors can detect the boundary layer development, the transition to turbulence, separation, and reattachment. Likewise, hot-films on the endwall of an LPT passage detected where a transitional boundary layer redevelops in the passage after the passage vortex [Vera et al. 2009].

1.2 Passage Flow Structures

There are several flow structures that form at the endwall through the passage of high-lift turbine blades. Sieverding [1985] and Langston [2001] have produced reviews on the research of

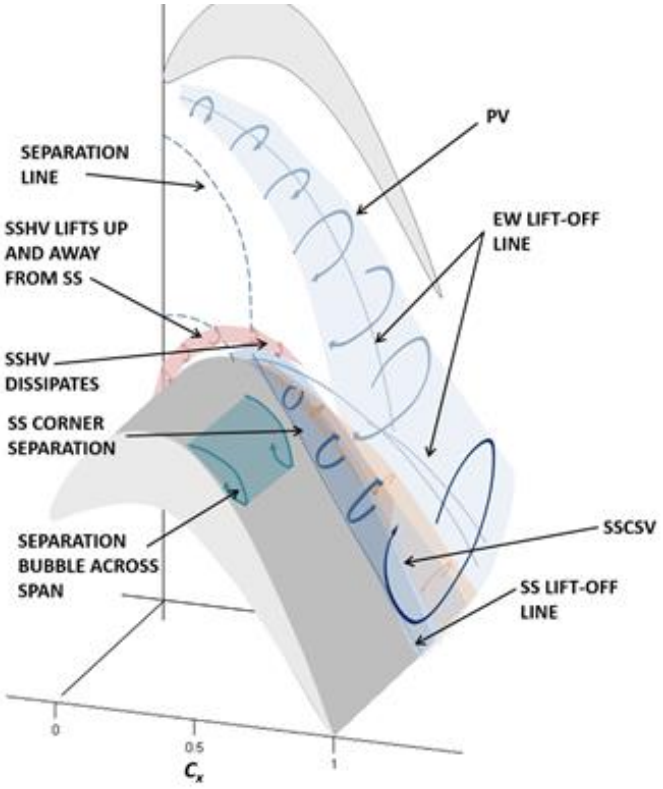

Figure 1-1. L2F flow field diagram (Marks 2016).

the secondary flow structures in a turbine passage. As with any junction flow with a blunt body, a horseshoe vortex (HV) forms. There are two legs of the HV, one on the suction side (SS) of the blade and the other on the pressure side (PS). The SS leg of the HV (SSHV) remains near the SS of the blade; in contrast, the PS leg of the HV (PSHV) is driven by the passage pressure gradient from the PS of the blade at the leading edge (LE) to the near SS of the adjacent blade by the trailing edge (TE), and is consequently also known as the passage vortex (PV).

In the high-lift front-loaded blade of interest in this investigation, the L2F, the SSHV dissipates prior to traversing very far down the passage; however, a new vortex forms called the suction side corner separation vortex (SSCSV), which has the opposite sense of rotation than the SSHV. The features of the L2F flow field are depicted in Figure 1-1. The PV and the SSCSV are rotating in the same direction; consequently, at their intersection, the two vortices are forcing the flow in opposite directions. This increases the size of the vortices and they climb the SS, causing an increase in endwall losses.

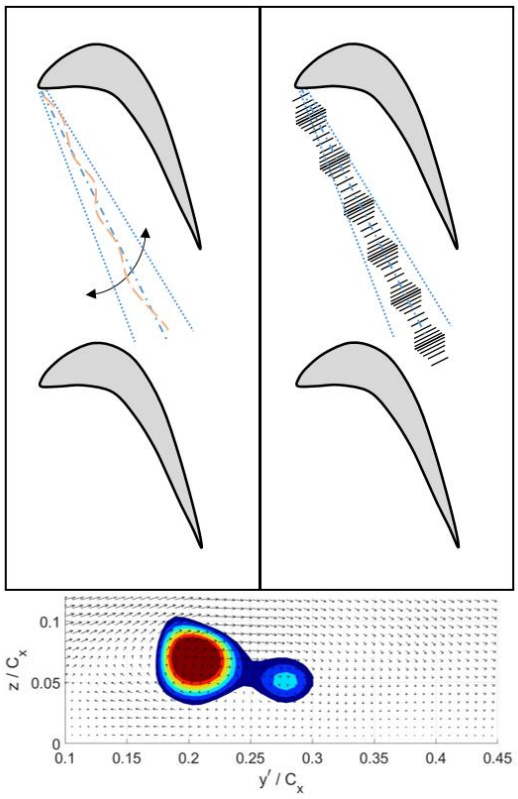

Figure 1-2. Top Left: PV sweeps pitchwise, Top Right: PV varies in speed and size, Bottom: PV can have two cores (bottom).

The HV is a common junction flow feature and has been studied fairly extensively. Praisner and Smith (2006) studied the HV of a faired cylinder to apply it to knowledge of LPT flow. They looked at the heat transfer on the endwall and the vorticity of the symmetry plane. They found that the secondary vortex is quasiperiodically ejected upwards creating a bimodal behavior in the HV. Consequently, the PV has the bimodal behavior, also described by Devenport et al. [1990] and Wang et al. [1997]. This bimodal behavior has been numerically captured by Gross et al. in the L2F passage [2016, 2017]. The bimodal behavior causes the PV to sweep pitchwise as it crosses the passage, Figure 1-2 (top left). The PV also varies in convection speed and size in the streamwise direction as it traverses through the passage, Figure 1-2 (top right). In the L2F passage, the PV also periodically loses coherence [Gross 2016, Veley 2018].

Around the vortices that predominated the endwall flow structures, there are several types of boundary layers. Vera found that downstream of the PV a transitional boundary layer reforms

[2009]. Likewise, Harrison also surveyed the different regions of the passage with commercial hot-film sensors and found that upstream of the PV is a transitional boundary layer, and that downstream of the PV toward the SS is a region of laminar flow which becomes transitional near the TE [1990]. Similar regions can be seen in the L2F passage in oil flow visualizations, Figure 1-3. A separated shear layer from the upstream region feeds the PV.

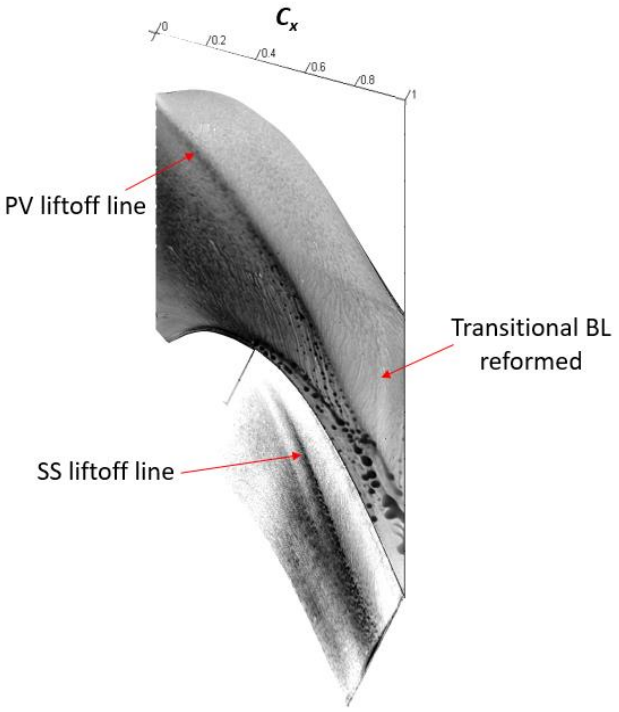

Figure 1-3. Oil flow visualization shows the average flow positions (Marks 2016).

A common occurance in blunt body flows is bursting, where quasiperiodically the fluid near the surface erupts into the flow above [Kline et al. 1967, Pope 2000, Sabatino et al. 2009]. Vortex bursting is a related process. A vortex burst is a sudden breakdown of the core, usually resulting in a bubble or spiral around the original vortex axis which eventually desolves into turbulent flow. [Lambourne et al. 1961, Heron et al. 2009]. Although most studies on vortex bursting have been executed using a delta wing [Lambourne et al. 1961, Soltani et al. 1993, Heron et al. 2009], a similar phenomenon occurs in the highly-loaded LPT passage. In the L2F passage, the PV quasiperiocically bursts or looses coherence (Gross et al. 2016). At instances of a PV burst the large vortex core is absent from the flow. Unlike the delta wing where the vortex bursts at a consisitant location, the bursting event in the LPT passage is complicated by the presence of the incoming shear layer, the passage cross-flow, and the bimodal nature of the PV.

1.3 Current Work

The goal of this research was to investigate the unsteady characteristics of the endwall flow structures in an L2F cascade, with focus the PV and its bimodal behavior. Comparisons were also made between the experimental results and the numerical studies completed by Gross et al. [2016, 2017].

The main tool used to obtain the unsteady characteristics was surface-mounted hot-film sensors which were manufactured in-house. This research into the unsteady PV characteristics expanded as the ability to use the hot-films was validated and improved. The capabilities of the sensors is explored in Appendixes A and B. The results will be presented first with a consideration of simultaneous hot-film signals acquired pitchwise and streamwise through the passage. Then it will correlate hot-film signals with concurrent flow visualization to create the connection between signal characteristics and major flow structures.

In summary, the objectives are:

- Develop and verify the application of in-house fabricated surface-mounted hot-films to the LSWT facility's linear cascade tunnel experiments (Appendixes A and B)
- Characterize the junction flow behavior through high-lift turbine blade passages
    - Upstream flow disturbance propagation downstream
    - Correlation of the unsteadiness between locations in the passage
    - Quantify the effect of FSTI on the endwall flow structures
- Characterize the transient behavior of the PV: pitchwise sweeping, bursting, and streamwise wavelength prior to bursting
    - Compare numerical simulation results to experimental
    - Use flow-visualization in conjunction with the hot-films to link hot-film signal signatures to specific structures and events

2. Experimental Arrangement

2.1 Facility

All experiments were conducted in AFRL's Low-Speed Wind Tunnel (LSWT) facility at Wright Patterson Air Force Base (WPAFB). The LSWT facility includes two open-loop wind tunnels: the linear cascade, Figure 2-1, and the developmental tunnel. The developmental tunnel has a test section that is 30.5cm x 30.5cm x 70cm (12in. x 12in. x 24in.) and is used to develop new measurement techniques; the linear cascade is used to study turbomachinery aerodynamics, with experiments that have recently been focused on the fluid dynamics that occur on the endwall of a low-pressure turbine passage.

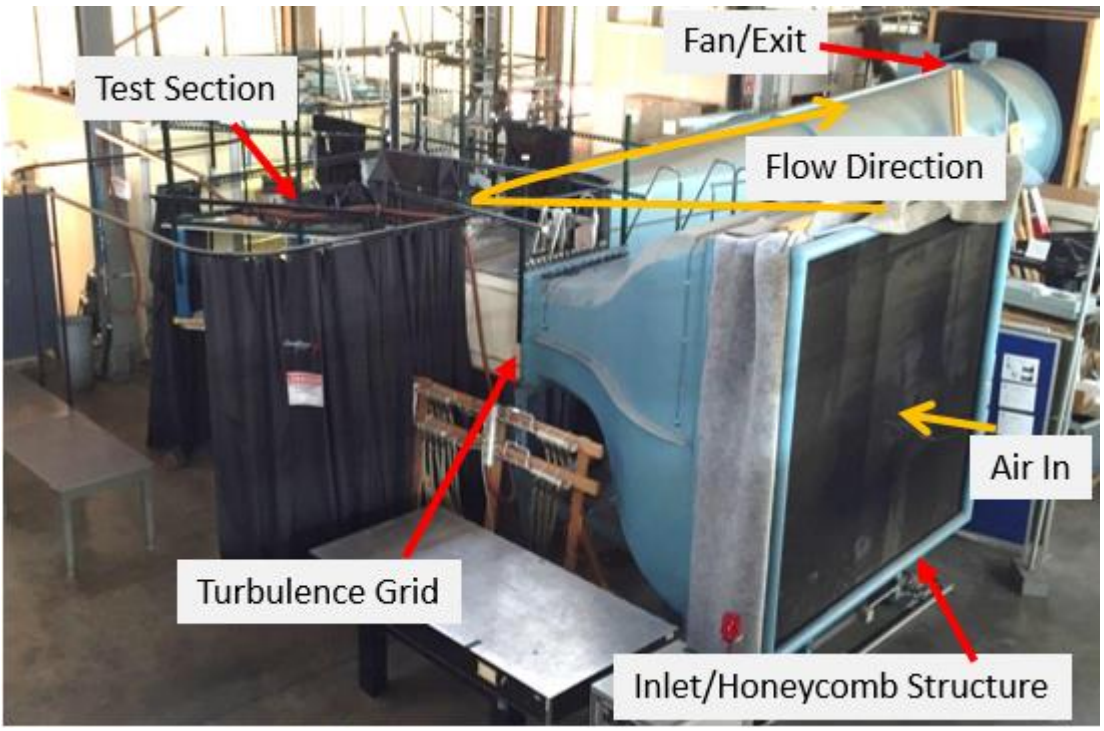

Figure 2-1. Linear Cascade Tunnel

The linear cascade pulls in air with an axial fan positioned at the exit. The 3.0m x 2.7m (3.3yd x 3.0yd) rectangular bell-mouth inlet of the tunnel has a honeycomb structure and an 8:1 area contraction ratio, resulting in low turbulence levels and uniform flow at the inlet to the test section. A removable turbulence grid following the honeycomb flow straightener allows for an increase in the freestream turbulence intensity (FSTI). The turbulence grid is constructed of 25.4mm (1in.) diameter horizontal and vertical cylinders spaced at 76.2mm (3in.).

The linear cascade for the experiment includes 7 straight highly-loaded low-pressure turbine blades, designed at AFRL using a system described in Clark et al. [2010]. The front-loaded L2F blade profile has superior midspan performance at low Reynolds numbers [McQuilling 2007]; consequently, the majority of losses occur at the endwall. The recent focus of the LSWT Facility has been to understand the endwall junction flow and reduce losses that are produced in that region.

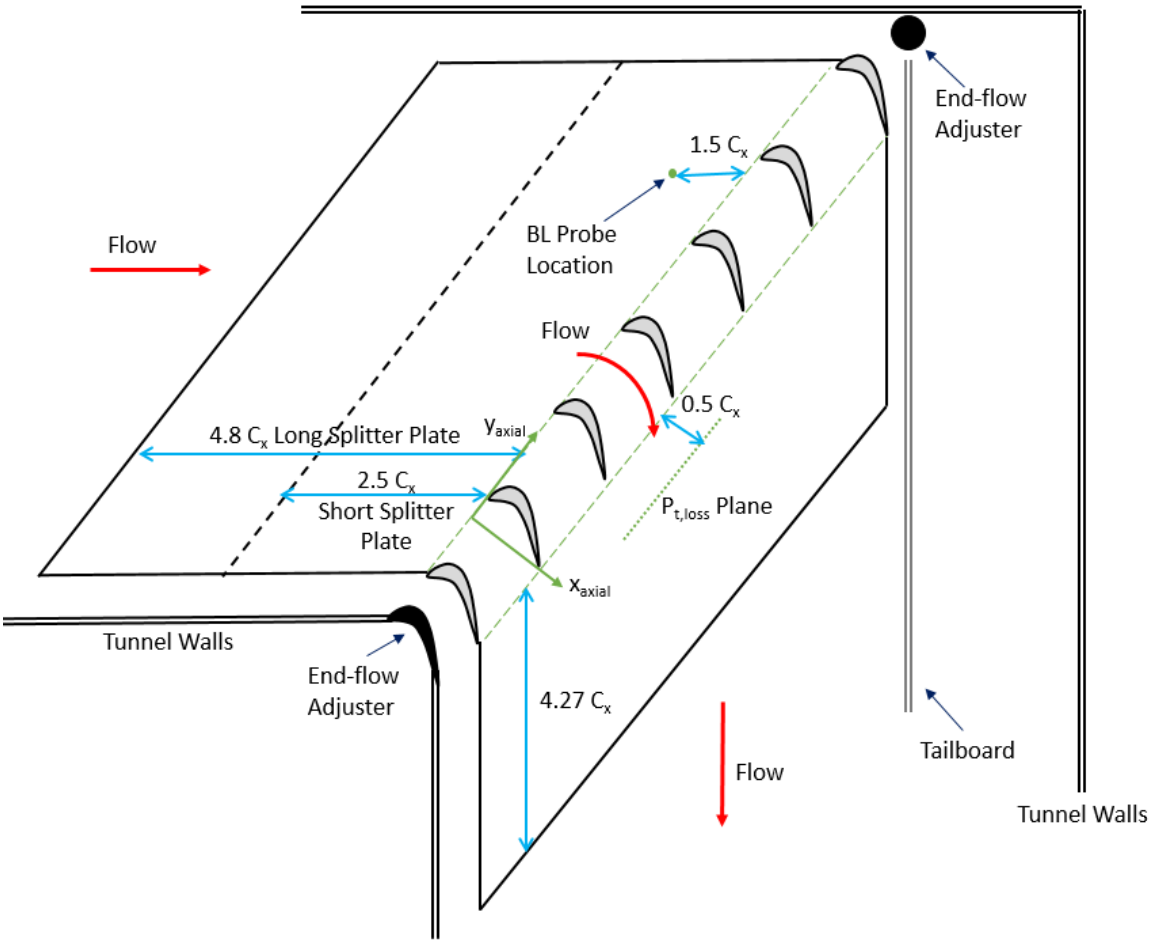

Figure 2-2. Top view of linear cascade test section.

The test section, depicted in Figure 2-2, has a splitter plate that allows control of the boundary layer thickness entering the cascade. Two splitter plate inlet section lengths were used in this study: $2.5C_x$ and $4.8C_x$ upstream of the leading edge. Most of the tunnel walls around the test section and the splitter plate are made of either clear polycarbonate (Lexan) or Acrylic, allowing for optical access into the test section.

The L2F blades have an axial chord (C_x) of 15.24cm (6in.) and are spaced to have a pitch to axial chord ratio of 1.221. The blades have a large turning angle from 35° entering the passage (off the axial direction) to -58.12° exiting the passage. The splitter plate can be moved in the spanwise direction, allowing for the cascade aspect ratio to be adjusted. To mitigate the effects from the junction flow from the top of the blade, a large aspect ratio of 4.17 is used, creating a distinct 2D midspan flow region. The cascade properties are summarized in Table 2-1.

Table 2-1. Linear Cascade Properties

Axial Chord, C_x	15.24 cm
Pitch/Axial Chord, S/C_x	1.221
Span/Axial Chord, H/C_x	4.17
Inlet Flow Angle (from axial), α_{in}	35°
Predicted Mean Profile Exit Angle, α_{out}	-58.12°
Streamwise Integral Length Scale, $L_{in,st}$	0.26 C_x
Zweifel Coefficient	1.59

2.2 Measurement Techniques

Throughout this study, several measurement techniques were used to obtain information about the flow field. These techniques include hotwire anemometry, surface-mounted hot-film measurements, stereographic particle image velocimetry (SPIV), and pressure surveys.

2.2.1 Hotwire Anemometry

Hotwire anemometry measures point velocity in a flow field based upon the convective heat transfer from a heated sensor element [Bruun 1995]. An electrical current heats a nickel or

platinum wire or a film deposited on a thermally insulating quartz rod. There are two types of anemometry: Constant Current Anemometry (CCA) and Constant Temperature Anemometry (CTA). A CTA system was used in this study. A CTA system uses a sensor element which is held at a constant temperature above the ambient temperature of the flow. A Wheatstone bridge adjusts the voltage supplied to the sensor, maintaining the resistance and consequently the temperature of the sensor. The voltage across the sensor, E_w, required to hold a fixed resistance is related to the velocity of the flow over the sensor by King's Law,

$$Nu\left(\frac{T_w}{T_f}\right)^m = A\,Pr^p + B\,Pr^q\,Re_d^n, \tag{2.1}$$

where *A*, *B*, *m*, *n*, *p*, and *q* are constants, $T_f = {}^{(T_w + T_a)}/_2$ is the film temperature, the Reynolds number is based on the sensor diameter, and the Nusselt number is

$$Nu = \frac{E_w^2}{R_w \pi l k (T_w - T_a)}, \tag{2.2}$$

where R_w is the set resistance of the heated sensor, T_w is the heated wire temperature, T_a is the temperature of the ambient fluid, *l* is the length of the sensor, and *k* is the thermal conductivity of the fluid [King 1914, Kramers 1946, Collis 1958, George 1989]. Substituting the Reynolds number and Nusselt number into Equation 2.1 gives

$$\frac{E_w^2}{R_w(T_w - T_a)}\left(\frac{T_w}{T_f}\right)^m = AkPr^p + k\left(\frac{\rho}{\mu}\right)^n BPr^q U^n, \tag{2.3}$$

where the values of *l*, *d*, and π are incorporated into the constants *A* and *B*. Classically, $m = 0.17$, $0.45 \leq n \leq 0.5$, $p = 0.2$, and $q = 0.33$ [George 1989].

In the LSWT facility, slightly different constants are used in King's Law and is described in detail by McQuilling [2007]. The Nusselt number is defined as

$$Nu = \frac{E_w^2\,R_w\,Pr^{-1/3}}{(R_w + 10)^2 \pi l k (T_w - T_a)}\left(\frac{T_f}{T_a}\right)^{TPR}, \tag{2.4}$$

where *TPR* is the temperature power ratio that is provided by the anemometer manufacturer. The Reynolds number is then calculated by

$$Re = \left(\frac{Nu-A}{B}\right)^{1/C_{exp}}, \tag{2.5}$$

where C_{exp} is the experimentally determined Reynolds number of the bulk fluid flow. The local velocity can be backed out of Equation 2.5 to get

$$U = \frac{Re\,\mu}{\rho\,d}. \tag{2.6}$$

Both the hotwire and surface-mounted hot-film sensors were operated using a TSI IFA 300 and controlled using an in-house LabVIEW code.

There are several ways to calibrate CTAs. The most common method, and that which is used in the LSWT facility, utilizes a jet with known velocity. The hotwire is placed in the jet stream at the same angle, e.g. vertical or horizontal, as it will be in the experimental flow. The jet is created through a pressure differential measured with a pressure transducer. This is used to calculate the Reynolds number. The voltage measured through the anemometer system is used to calculate the Nusselt number. When *Re* is raised to the C_{exp} the relationship becomes linear

$$Nu = A\left(Re^{C_{exp}}\right) + B. \tag{2.7}$$

Obtaining data points at various velocities in the range of application allows the constants *A* and *B* to be calculated through a linear regression, such as the least square method.

Once calibrated, this investigation used hotwires to measure the FSTI. The FSTI is calculated using the velocity

$$FSTI = \frac{\sqrt{\frac{1}{N}\sum(U-\bar{U})^2}}{\bar{U}}, \tag{2.8}$$

where N is the number of data points. To measure the velocity to calculate the FSTI, the hotwire was positioned $1.4C_x$ upstream of the row of blades and $0.10H$ above the splitter plate. The sampling rate was set to 160Hz and two 5min data sets were acquired at four Reynolds numbers

(30k, 50k, 75k, and 100k). The FSTI was determined to be 0.9% without the turbulence grid in the cascade and 3.1% with it present.

Initially, a hotwire was used in conjunction with a surface-mounted hot-film. This was done to insure the surface-mounted hot-film obtained similar results to the hotwire when placed in the same flow field. Appendix A shows this in a cylinder and flat-plate flow, while Appendix B shows preliminary measurements in the cascade.

2.2.2 Surface-Mounted Hot-Film Sensors

The surface-mounted hot-films used in the LSWT facility are manufactured in-house. The initial use of the sensors was in a constant current mode to make heat flux measurements on a single stage turbine rig based on surface temperature changes. Since the LSWT facility is essentially isothermal, the hot-films were used in a constant temperature mode to measure fluctuations in shear stress with high temporal resolution. Appendix A and B provides additional details on the development of the hot-films for this purpose.

Hot-films have been used to measure the locations of transition, separation, and reattachment within boundary layers [Nakayama 1993, Zhang 2002]. The voltage fluctuation can be used to calculate quasi-shear stress,

$$\tau_q = \left(\frac{E_w^2 - E_0^2}{E_0^2} \right)^3 , \tag{2.9}$$

where E_0 is the voltage drop across the sensor under a no flow condition.

For the experimental setups that involve using an array of hot-films, the hot-films sensors were spaced at 5mm (0.20in.) intervals, see Figure 2-3. The hot-films are operated with a TSI IFA 300 CTA. The IFA 300 has the ability to implement high-pass and low-pass filters at a limited set of frequencies, and also has adjustable gains for each channel. The greatest sampling rate the DAQ system allowed was 15kHz per channel when all channels are in use; this allowed for a low-pass filter of 5kHz, which matched the sampling rate of the high-speed flow visualization. The hot-films were operated with an overheat ratio of 1.2, which is low compared to values in literature for

surface-mounted hot-film applications. The overheat ratio was kept low to prevent the acrylic splitter plate from melting. When a gain other than one is set, the high-pass filter must be used, which in turn prevents the use of Equation 2.9, as the value of E_0 tends toward zero.

Note that although there are anemometers labeled as hot-films that are not surface-mounted. Throughout this thesis, the term "hot-film" will refer to the surface-mounted hot-film sensor produced at AFRL and the term "hotwire" will be used for anemometers.

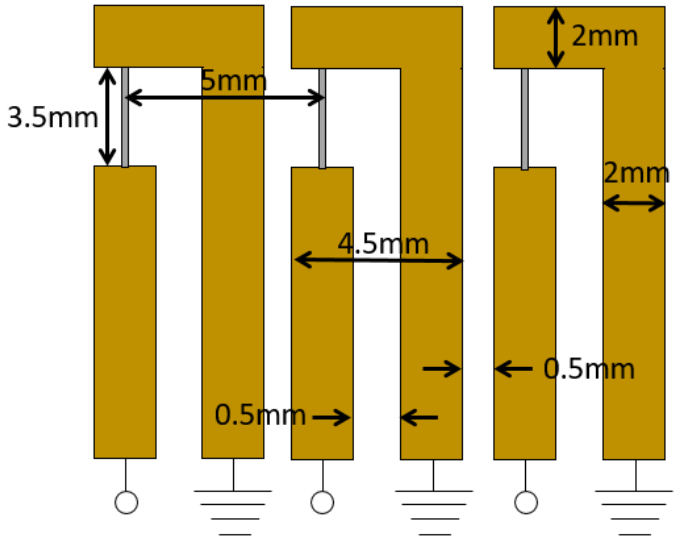

Figure 2-3. Hot-film array dimensions

2.2.3 Stereographic Particle Image Velocimetry

Stereographic Particle Image Velocimetry (SPIV) is a nonintrusive method to measure the three-dimensional components of velocity in a single plane of the flow field. SPIV uses a laser sheet to illuminate particles in the flow field. Two cameras are positioned to obtain two different view angles of the laser sheet, Figure 2-5. A timing unit triggers the laser to pulse twice with a certain time lag, *dt*, and the cameras to capture the image of the laser sheet at those times. The shift in location of a group of particles, see Figure 2-4, is calculated by breaking each frame up into smaller windows, then cross-correlating the corresponding windows between frames. Two velocity components are calculated from the particle shift between frames in each camera view. The third

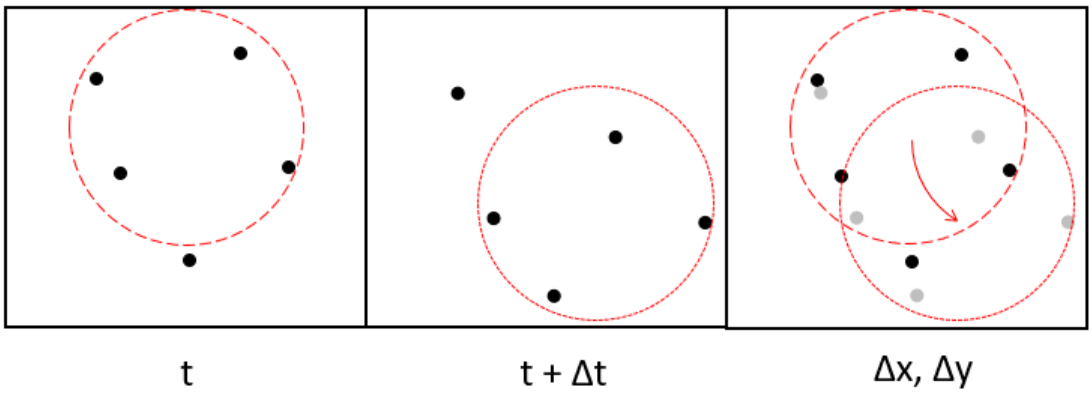

Figure 2-4. Shift of particle group between pulses during PIV

component of velocity can be calculated because the cameras are at different identified angles. The result is a plane with all three velocity components.

The LSWT facility has two SPIV systems, a low-repetition rate system and a high-repetition rate system. Both systems use LaVision's programmable timing unit (PTU) and software (DaVis 8.3 for slow-rep, DaVis 8.4 for high-rep). The low-rate system can take images up to 15Hz, whereas the high-rate system can take images at rates greater than 1000Hz. The frequency of the

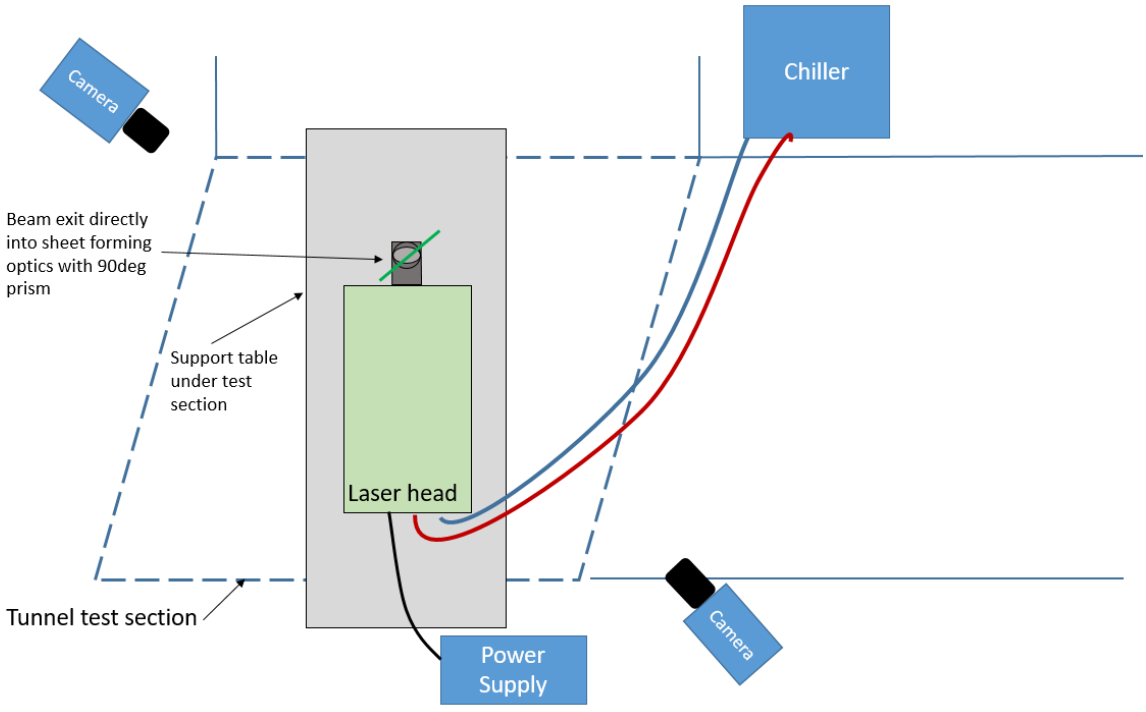

Figure 2-5. SPIV set-up for the linear cascade.

high-rate system can be increased by reducing the portion of the camera's sensors that collects data. The slow-rate system uses a 200mJ dual head Quantel Evergreen laser and two LaVision sCMOS cameras (2560 x 2160 pixel resolution) fitted with Scheimpflug adapters. The high repetition rate system uses a Photonics Laser model DM30-527DH and Phantom VEO 640L cameras (2560 x 1600 pixel resolution) also fitted with Scheimpflug adapters. The cameras are calibrated with a two surface 106-10 LaVision calibration plate. To increase the rate of images in the high-speed system the resolution of the VEO 640L cameras was decreased to 1418 x 964 pixels. This allowed for a single frame rate of 5kHz, used for flow-visualization, and allowed for a double frame rate of 2.5kHz, used for PIV. The time lag between images in the double frame mode was 10μs. For the low-rep system at least 100 images were captured to calculated the mean flow, whereas, 5200 images were acquired for the high-rep system, which insured the ability to obtain independent samples.

For both systems, either a Concept Smoke ViCount oil smoke generator or an MCM Electronics fog generator was used to seed the flow. For flow-visualization, creating images where the flow structures in the images are distinguishable to the naked eye requires over-seeding the flow field. This was done by using the ViCount with mineral oil, which produces particle diameters of less than a micron, which is too small for effective use with PIV.

2.2.4 Pressure Measurement

Pressure measurements are used in several ways in the linear cascade: for quantifying inlet air velocity, boundary layer measurements, and passage total pressure loss measurements.

A Pitot-static probe, positioned $2C_x$ upstream of the passage, measures the incoming freestream velocity which is used to calculate the Reynolds number by which the tunnel speed is set. A 0 to 0.4 inH_2O Druck Pressure Transducer is used in conjunction with a NI PXI-1052 Chassis with a SCXI-1305 card to acquire the data. The flow is considered incompressible and Bernoulli's equation for incompressible flow is used to calculate the incoming velocity,

$$P_t = P_s + q = P_s + \frac{1}{2}\rho U^2. \tag{2.10}$$

To measure the boundary layer in different flow regimes, a boundary layer probe was positioned $1.5C_x$ upstream of the passage. A hole in the splitter plate was used as a static pressure tap. A -0.2 to 0.8 inH_2O Druck pressure transducer was used. The boundary layer probe was traversed up 2cm from the splitter plate taking 60 evenly spaced data points. The momentum thickness of the boundary layer is calculated using

$$\theta = \int_0^\infty \frac{u(z)}{U_\infty}\left(1 - \frac{u(z)}{U_\infty}\right) dz. \tag{2.11}$$

The displacement thickness is calculated using

$$\delta^* = \int_0^\infty \left(1 - \frac{u(z)}{U_\infty}\right) dz. \tag{2.12}$$

The shape factor of the boundary layer is

$$\mathcal{H} = \frac{\delta^*}{\theta}. \tag{2.13}$$

For flow over a flat plate the shape factor is 2.6 for laminar flow and 1.3 for turbulent [White 1999]. A favorable pressure gradient causes the shape factor to decrease and the skin-friction coefficient to increase and could cause the boundary layer to relaminarize [Pope 2000]. Conversely, an adverse pressure gradient would cause the mean velocity profile to flatten, the shape factor to increase, the skin-friction coefficient to decrease, and could cause the boundary layer to separate [Pope 2000]. For laminar flow, separation can occur at a shape factor of roughly 3.5, and for turbulent flows at roughly 2.4 [White 1999].

The total pressure loss in the passage is the primary method of determining the effectiveness of flow control. The total pressure loss coefficient is calculated using

$$\gamma_t = \frac{P_{t,in} - P_{t,out}}{\frac{1}{2}\rho U_{in,s}^2}. \tag{2.14}$$

Downstream total pressure measurements were acquired with a pressure rake containing five inline Kiel probes. The probes were each connected to a 0 to 1 inH_2O AllSensor pressure transducer, with the differential pressure port connected to the total pressure port from the upstream Pitot-static probe. The rake was located $0.5C_x$ downstream from the trailing edge of the blades, as shown in Figure 2-2. The probes were traversed across a pitch and up to half span, creating a grid of 30x30 data points. The total pressure loss of the passage is calculated using the integral of Equation 2.14 over the area, creating the area-averaged total pressure loss coefficient non-dimensionalized by $S \cdot H$.

2.3 Methodology

This investigation progressed over several stages. The first stage used a single hot-film at various locations throughout the passage and was compared with a co-located hotwire signal, which is contained in Appendix B. The second stage simultaneously acquired data with hot-film arrays of up to eight sensors. The final stage used concurrent flow-visualization with the hot-films to correlate the flow structures with the hot-film signal.

Data was collected under a variety of tunnel conditions. The use of both splitter plates and the turbulence grid allowed for up to four test conditions at a given Reynolds number (high and low turbulence, thin and thick boundary layer); however, it was determined through PIV measurements and some initial hot-film measurements that the flow structures did not change enough to make all four cases worth exploring. It was decided to eliminate the case with the short splitter plate and the turbulence grid, where the main difference was the boundary layer thickness. The remaining three cases, identified as flow conditions A thru C, are summarized in Table 2-2. The numerical simulation conducted by Gross [2017] matched the boundary layer and the Reynolds number of flow condition A, but did not match the FSTI, which was zero in the computation.

With the lower FSTI, the flow was found to separate at midspan at lower Reynolds numbers. This limited the study to a Reynolds number of 100k. The Reynolds number for setting the tunnel flow speed is based on the midspan inlet velocity and the axial chord.

Table 2-2. Flow conditions.

Flow Condition	Splitter Plate Length	FSTI	Inlet $\delta_{99\%}$ (%C_x)	Inlet $\delta_{99\%}$ (%H)	Inlet Shape Factor, $\mathscr{H}$	γ_{ps}
A	Long	3.0%	9.3	2.2	1.5	11.5
B		0.9%	7.3	1.7	1.7	12.0
C	Short	0.9%	1.8	0.4	1.8	10.1

2.3.1 Simultaneous Hot-Film Sensors

This section discussed the simultaneous use of multiple hot-film sensors. A total of twenty-two flexible sensors were situated on the endwall of the passage, on the suction surface of the blade, and upstream of the blade passage. Locations were determined based on oil flow visualization, SPIV, and hotwire results under flow condition A from Table 2-2. All three flow conditions were investigated in this section. The main focus of the locations chosen was based on interest in the PV as it forms at the leading edge and propagates through the passage and interacts with the suction surface and corner separation. The locations of the arrays on the endwall are depicted in Figure 2-6. The location of the sensors on the SS is shown in Figure 2-7. The location of every sensor for the simultaneous hot-film measurements is summarized in Appendix C.1.

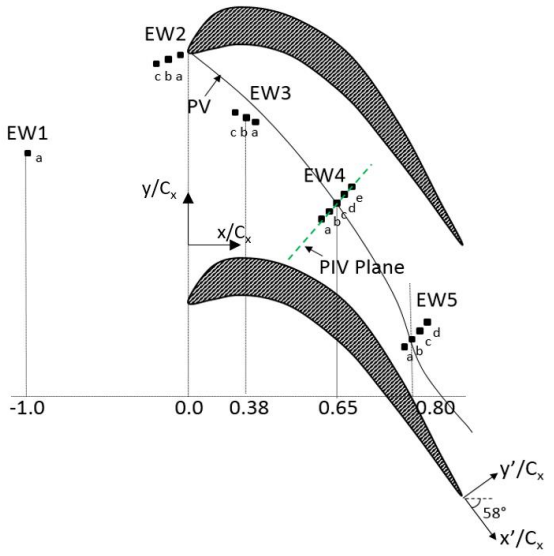

Figure 2-6. Schematic of hot-film locations for simultaneous data acquisition.

Sensors were distributed in arrays of one to five sensors, with each

platinum sensor spaced at 5mm intervals. See Figure 2-3 for array dimensions. Particular care was taken in routing the signal wires, preventing the wires from disturbing the flow of neighboring sensors.

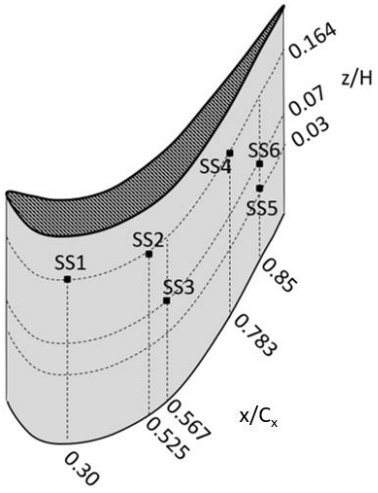

Figure 2-7. Hot-film sensor locations on the suction surface.

The naming convention of the arrays used three elements: the surface, the array, and the sensor. The endwall surface is denoted by 'EW' and the suction surface is denoted by 'SS.' The arrays are numbered, started with 1 as the furthest upstream with each subsequent number being the next array downstream. The sensors were designated with lowercase letters, with 'a' being the leftmost sensor when looking from downstream towards upstream which was also up the leads of the array. Therefore, the sensor 'EW4b' is in the fourth array on the endwall second sensor from the left. Figure 2-8 gives an example of the naming convention.

Figure 2-8. Array naming convention.

Up to eight hot-films could be measured simultaneously, limited by the number of IFA 300 channels available. To compensate for the low overheat ratio, a gain was applied to each sensor ranging from 2 to 20 as was determined during preliminary runs for each sensor. The gain was applied to allow for full range of the analog-to-digital converter (ADC) to be used; consequently, a 0.1Hz high-pass filter was used. A 2kHz low-pass filter was used, and the sampling rate was 8kHz. For each set of sensors operated, two 30 second samples were recorded for every flow condition. Each set of data obtained was focused either on the streamwise movement of the PV or the pitchwise movement.

2.3.2 Concurrent Hot-Film and Flow Visualization

To obtain a better understanding of what the signal signatures represent, concurrent hot-film and flow visualization was obtained.

Prior to using the hot-films concurrently with the laser, the minimum distance between the laser sheet and the hot-film sensors had to be determined so that the hot-films would not sense the laser pulses. A hot-film was secured on a cantilever arm mounted on a traverse. The hot-film was then positioned facing downwards toward the bottom of the test section in line with the laser sheet. The Evergreen laser was pulsed at 10Hz with 50% power. The hot-film was moved downstream in the passage until it no longer picked up the 10Hz pulse. It was found that the platinum sensing element had to be 5mm from the laser sheet before the laser was undetectable.

To synchronize the hot-film and PIV system two methods were used. For the low-speed PIV system, a hot-film was mounted to the bottom of the tunnel directly under one of the blades and in-line with the laser sheet. This hot-film was used to sync the flow-vis and hot-film data. Whenever the laser pulsed, the hot-film voltage signal recorded a downwards spike; however, this method required the use of a channel in the CTA leaving only seven channels for data acquisition in the tunnel passage. This method also did not work with the high-speed PIV system, as the high-speed energy of the laser on the hot-film reverses the process of sputter deposition that was used to

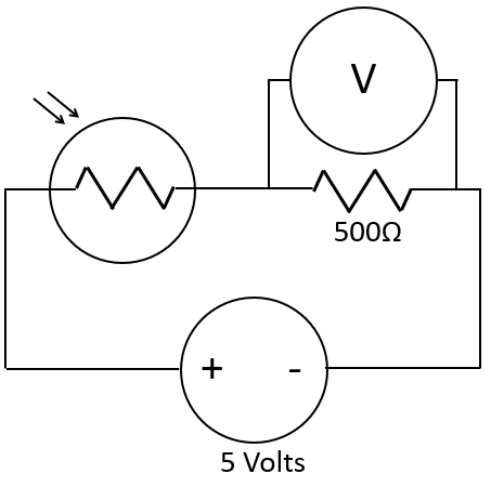

Figure 2-9. Photo resistor circuit.

create the hot-films. Therefore, with the high-speed PIV system, a photo resistor circuit was used, Figure 2-9. A photo resistor and 500Ω resistor in series were supplied by a 5V voltage source. The reflections from the laser pulse caused the resistance of the photo resistor to increase, thereby decreasing the voltage across the 500Ω resistor, which was recorded by the DAQ card. Each voltage drop indicated a laser pulse. However, the high-speed PIV system pulsed the laser for an indeterminate amount of time before and after the images were acquired to insure laser stability; therefore, an indication of which laser pulse corresponded to the first image was required. This was accomplished by recording the trigger that starts the image acquisition. An Agilent 33220A function generator was set to a pulse wave with an edge time of 5*n*s and an amplitude of 5V. The output signal went to both the DAQ card and the trigger input on the PTU. The change in the signal is detected and the next laser pulse read from the photo resistor circuit corresponds to the first image captured. This is depicted in Figure 2-10, where the downward spike of the photo resistor indicate the laser pulse and the step in the function generator signal indicates the trigger to start image acquisition. Therefore the uncertainty in the alignment of the hot-film signals to the images is less than 0.07ms.

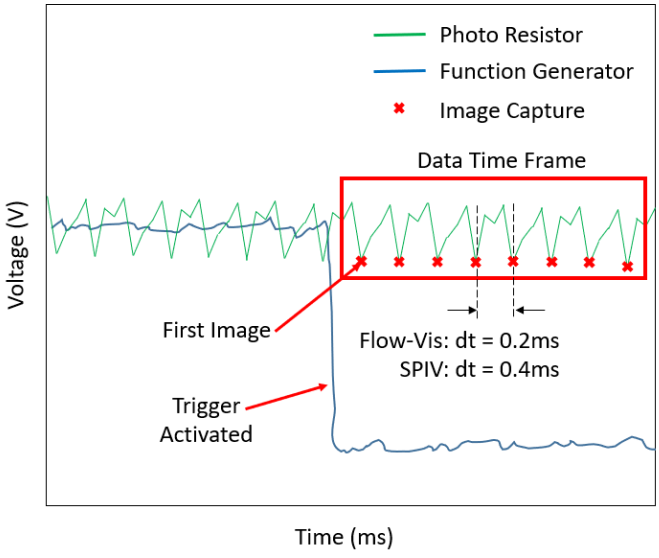

Figure 2-10. Example of synchronizing voltages with the flow visualization and SPIV images

The area of interest was similar to the EW4 region in the simultaneous hot-film study. The array of hot-film sensors was parallel to the laser sheet which was perpendicular to the exit flow angle. The centers of the platinum sensors were located 19mm downstream of the laser sheet in the high-speed PIV setup, and 14mm downstream of the laser sheet in the low-speed PIV setup. This allowed the part of the copper leads that are positioned upstream of the platinum sensor to stay beyond the influence of the laser sheet. The array of hot-film sensors was positioned at x'/C_x = -1.03 and the laser plane at x'/C_x = -1.15. The plane of the laser sheet is the same plane the EW4 hot-film array described in Section 2.3.1. The locations of the hot-films is tabulated in Appendix C.

3. Results and Discussion

The results are organized by first presenting an brief overview of the numerical results. Next, the results of the simultaneous hot-film arrays will be expounded upon, analyzing the sensors distributed in both the pitchwise and spanwise directions, with a brief comparison to the numerical simulation. Finally, the hot-films and flow-visualization results will be presented, once again compared to the numerical simulation.

3.1 Numerical Simulation

The purpose of first presenting a brief overview of the numerical results is to provide a better understanding to comparisons with the experimental results presented later. There are two portions of the numerical data: that already published [Gross et al. 2016, 2017], and that not yet published but provided directly by Gross that was merely a continuation of the data published.

The numerical data is from an Implicit Large Eddy Simulation (ILES) with boundary conditions that most closely matched flow condition A described in Table 2-2 sans matching the FSTI, which was not modeled. The convective terms of the Navier-Stoke equations were ninth-order accurate, the viscous terms were fourth-order accurate, and the time advances used an implicit second-order accurate scheme. All parameters were non-dimensionalized for the simulation. Time was non-dimensionalized based on axial chord, Reynolds number, and kinematic viscosity,

$$t^* = \frac{t \times Re \times \nu}{C_x^2}. \tag{3.1}$$

The non-dimensionalized time is approximately 64.6 times the dimensional time. Similarly, frequency was non-dimensionalized using the same parameters:

$$f^* = \frac{f \times C_x^2}{Re \times \nu}, \tag{3.2}$$

which gives that the non-dimensional frequency is approximately 0.015 the dimensional frequency. The ILES results clearly show that the passage vortex periodically loses coherence, Figure 3-1. The

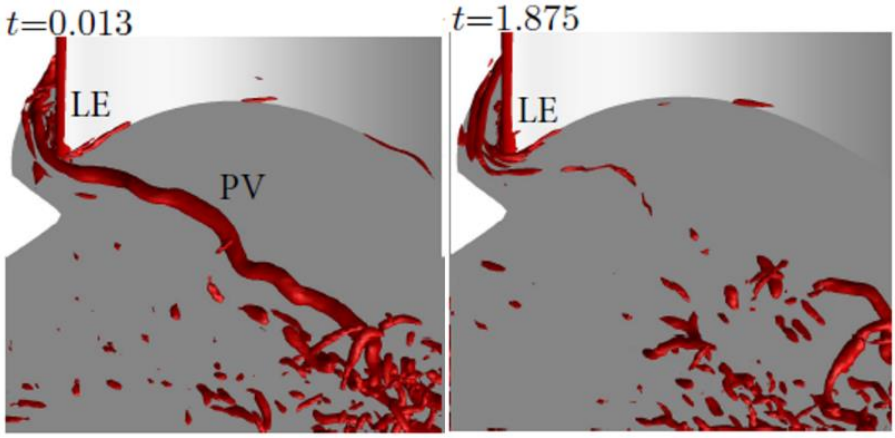

Figure 3-1. Transient behavior of the PV from ILES (Gross 2016). Left: PV core through the passage. Right: PV bursting event.

PV has a streamwise wavelength of 0.3 between bursting events, Figure 3-2 [Gross 2016].

The simulations have shown the PV is not stationary and shifts around in the passage in the pitchwise direction with undulation in the streamwise direction. The core of the PV shifts toward the pressure side, loses coherence, and then reappears closer to the suction side of the passage. The images in Figure 3-1 show the core of the PV (left) and the loss of coherence (right). The non-dimensional wavelength of the PV prior to bursting was found to be 0.3, Figure 3-2. If the vortex is assumed to convect between 0.5 and 0.8 times the local freestream velocity, the streamwise convective period would be roughly 1.23 to 1.94 (19ms to 30ms). The duration of the bursting event was roughly a non-dimensional time of 1.25 (19ms). Figure 3-3 shows the perturbations of kinetic energy over time in regions shown in Figure 2-6. There are peak disturbances in the signal that propagate

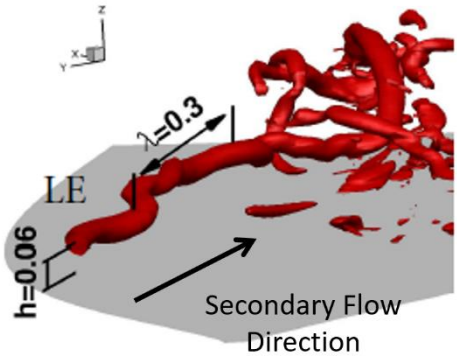

Figure 3-2. Streamwise wavelength of PV prior to bursting [Gross 2016].

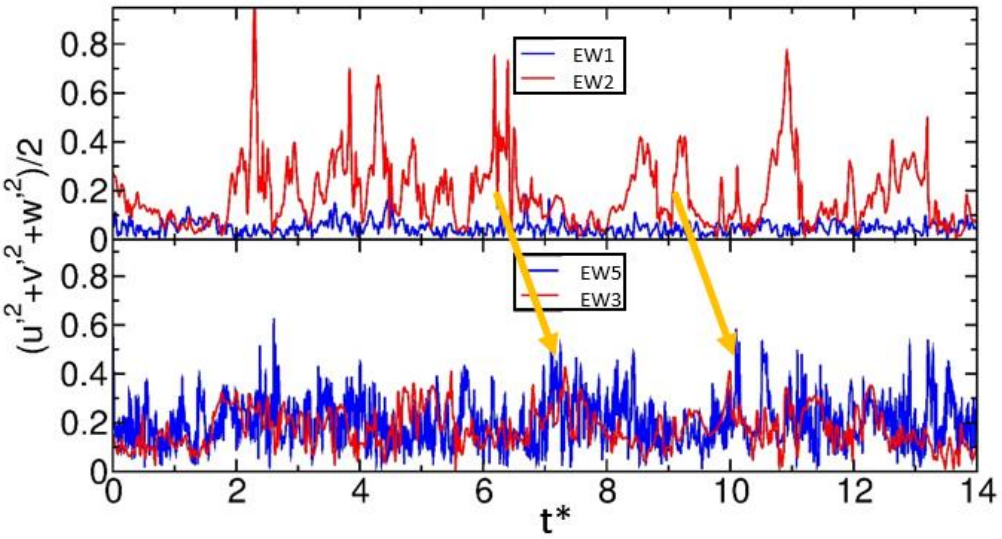

Figure 3-3. Disturbance time signal. Probes located at $z/C_x = 0.05$ [Gross et al. 2017].

downstream, shown with the arrows. The delay appears to be around a t^* of 1 (15.5ms). This would correspond to a non-dimensional frequency of approximately 1 (64Hz). The frequencies of the disturbance time signal, Figure 3-4, shows that the non-dimensional frequency peaks around 0.4 (26Hz). Similarly, a large peak in the PSD of the simulation's leading edge probe, probe 2, occurs at an f^* of 0.5 (32Hz). Wang et al. found a similar frequency with an f^* of 0.57 at a Reynolds

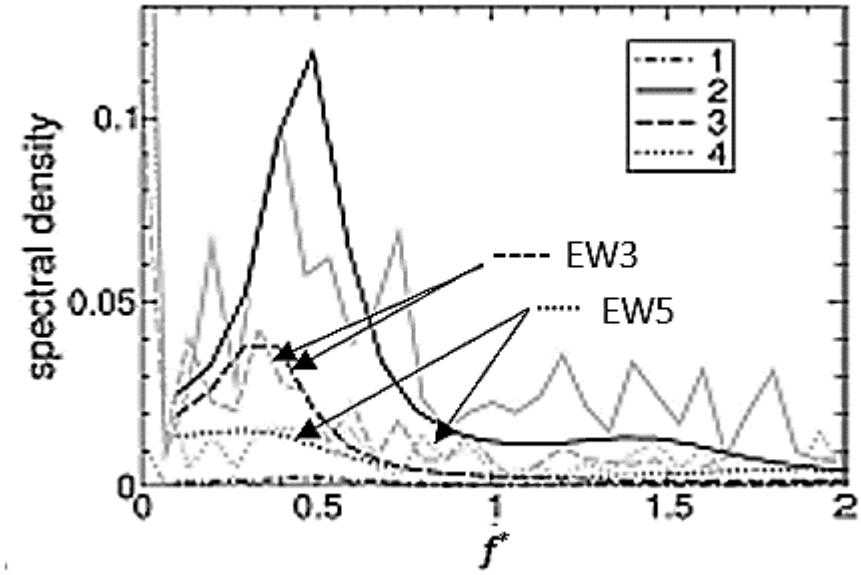

Figure 3-4. Numerical findings from ILES. Positions 3 and 4 correspond to regions EW3 and EW5 respectively. Light grey lines are the raw FFT with no windowing, the dark lines were calculated using the maximum entropy method [Gross et al. 2017].

number of 9900 based on inlet velocity and true chord [1997]. Gross et al. concluded that the leading edge junction flow showed a bimodal behavior and quasiperiodically losses coherence as a result [2017].

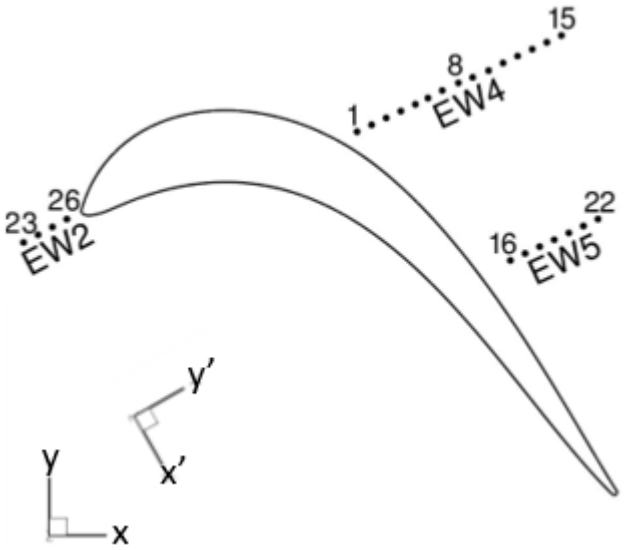

Figure 3-5. Sensor locations of second portion of ILES data.

The second portion of the ILES data had twenty-six probed positions, Figure 3-5. The probes are located essentially on the endwall at $z/C_x = 5\times10^{-5}$. The probes from the simulation are named using two parts, an 's' followed by the probe number as indicated in Figure 3-5. Probes s1 to s15 are in the EW4 region with s4 through s11 being in the same locations as sensors EW4a through EW4h as described in Section 2.3. Likewise, probes s16 to s22 correspond to the EW5 region, and probes s23 to s26 are in the leading edge region, EW2. The skin-friction components of the probes in the simulation located in the EW4 and EW5 regions were broken into the x'- and y'-coordinates. The y'-component best represented the signals of the hot-film sensors as that is the direction of the narrowest part of the platinum sensors that are in the array set-ups and therefore the hot-films were most responsive to flow changes in the y' direction. Similarly, the skin-friction data of the EW2 region probes were decomposed into the incoming flow angle, 35°, which was the most sensitive flow direction of the hot-film sensors located in the EW2 region. The mean signal was also removed prior to any data processing in order to look only at the signal fluctuation as was done with the experimental results.

The cross-correlation between s26, the sensor closest to the leading edge, and the rest of the sensors were calculated and shown in Figure 3-6. The stochastic nature of the flow causes the cross-correlation values to be low. The strongest correlation was with s13 at $t^* = 1.03$ (16ms), with

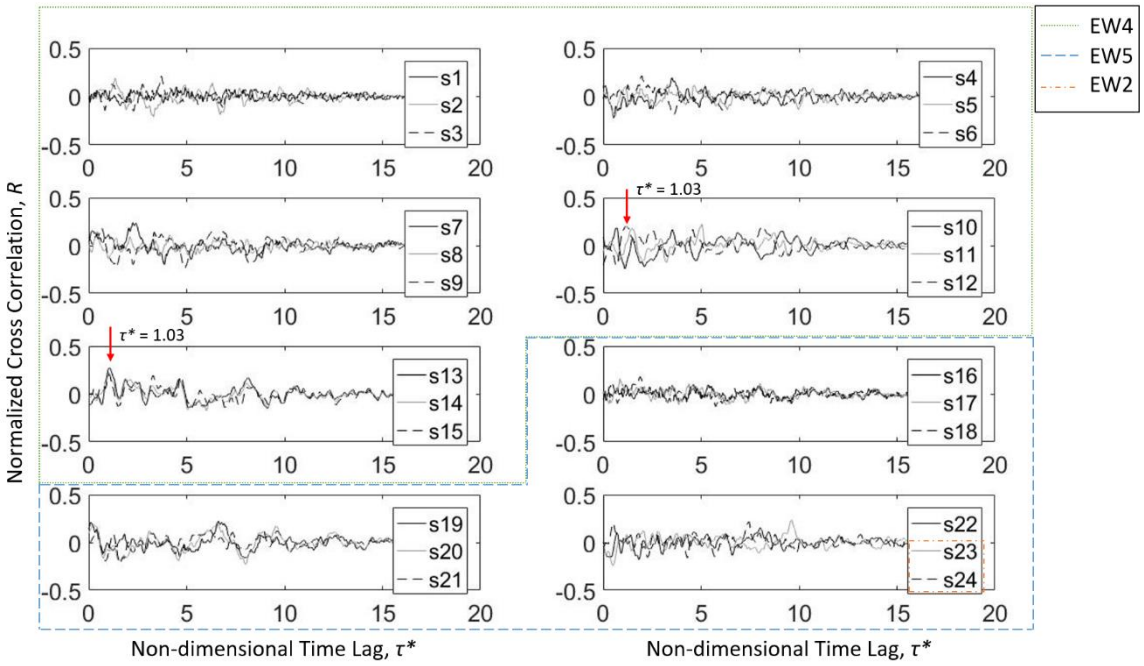

Figure 3-6. Cross-correlations with s26, the probe closest the leading edge, strongest correlation is at t = 1.03.*

the peaks at the same time lag for probes s12, s14, and s15. This implies that it takes approximately 1.03 (16ms) for the corresponding flow structure to propagate from the leading edge to the EW4 region. This corresponds to a non-dimensional frequency of 0.97 (62.5Hz). The distance from the EW2 region to the center of the EW4 array is 17cm and the distance from the EW2 region to the center of the EW5 region is 24cm. Substituting these lengths in as the characteristic length, the calculated the time lag is 1.3 to 2.4 (20ms and 38ms), respectively. Because it was found that the time taken to propagate from the EW2 region to the EW4 region is approximately 1.03 (16ms) it is reasonable to estimate that the convective speed of the endwall flow structure is 0.8 of the local freestream velocity as previously assumed.

Not only do signatures in the signal propagate downstream, they also appear to propagate pitchwise. The PV sweeps in the pitchwise direction which causes similarities in signals of adjacent probes. This can be seen in Figure 3-7, which shows fluctuations in the skin-friction in the y'-direction. Eleven points in time are identified in the signal. Each of these points have an associated skin-friction contour plot image in Figure 3-8, which also has isosurfaces that depict the location

of the PV. It is obvious that the three signals in Figure 3-7 are related as they all have an increase in the skin-friction at approximately t^* of 14.5. The contour plots show that the suction side of the PV has greater skin-friction than the pressure side. At the time of the first contour plot, the PV is nearer to the suction side and is sitting above s9, then it sweeps across the pitch sitting above s10

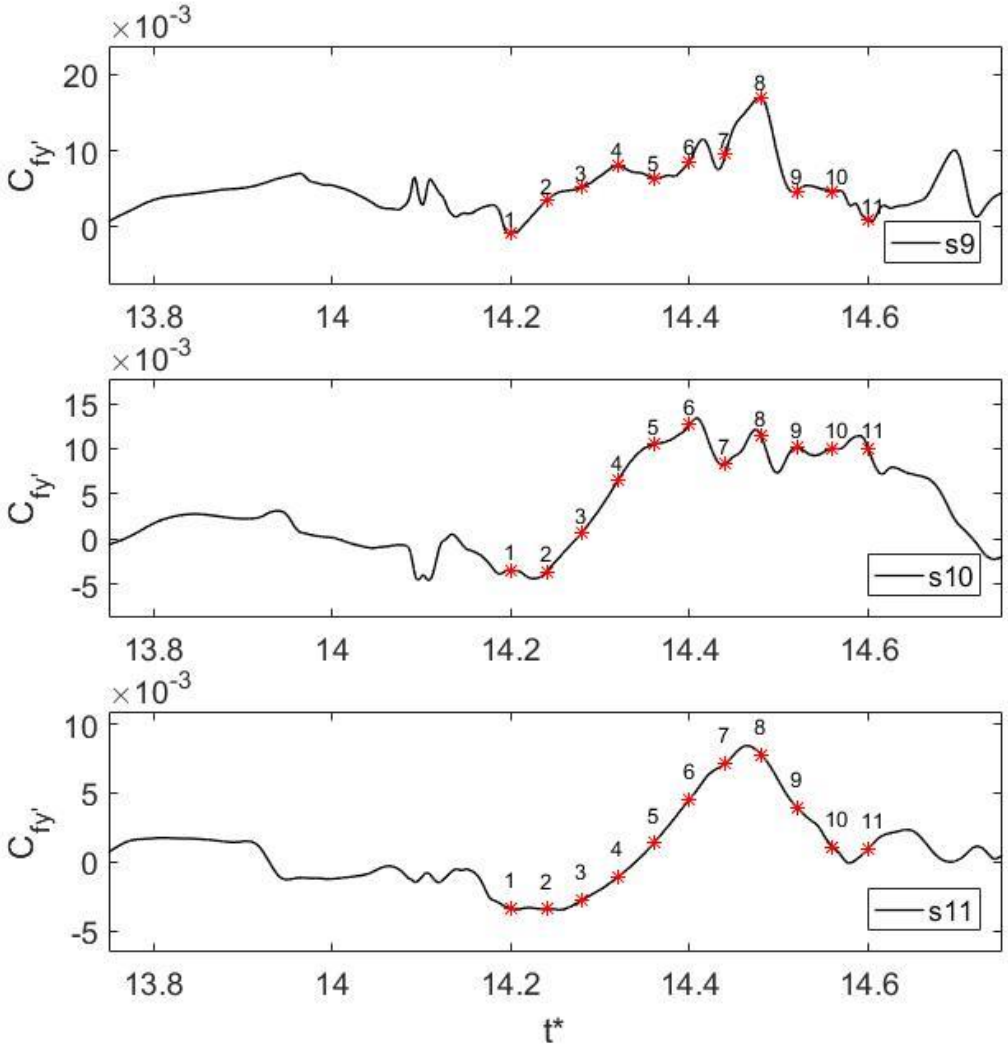

Figure 3-7. The skin-friction signal in the y'-direction. The numbered points correspond to the images in Figure 3-8.

in frame 3 and s11 in frames 4 and 5. The PV sits to the pressure side of s11 for frames 6 through 8, when it starts the sweep back to the SS. The signal of s11 shows a large peak when the PV was toward the pressure side, similarly both signals for s9 and s10 also increases when the PV core moves to their pressure side.

Alongside the suction side of the PV in Figure 3-8, the contours show a dual region of high skin-friction. Between the dual regions is a region of low skin-friction. For the time snapshots shown, s10 sits in this low region, s11 in the higher skin-friction region just to the suction side of the PV, and s9 is in the region of highest skin-friction. Of these regions, the probe furthest from the PV (closest to the suction side) has the greatest magnitude of skin-friction. Some decrease in magnitude occurs in both parts of this dual region when the PV develops strong vortical tendrils around it as can be seen in frame 7. These vortical tendrils propagate downstream and therefore illustrate the convection rate of the PV.

Although the bursting event can be clearly seen in the EW4 plane in the experimental flow-visualization and upstream in the ILES, by the time the flow propagates to the EW4 region in the numerical simulation, the PV has redeveloped. Therefore, no conclusions could be made of how the EW4 signal signatures relate to the loss of coherence of the PV.

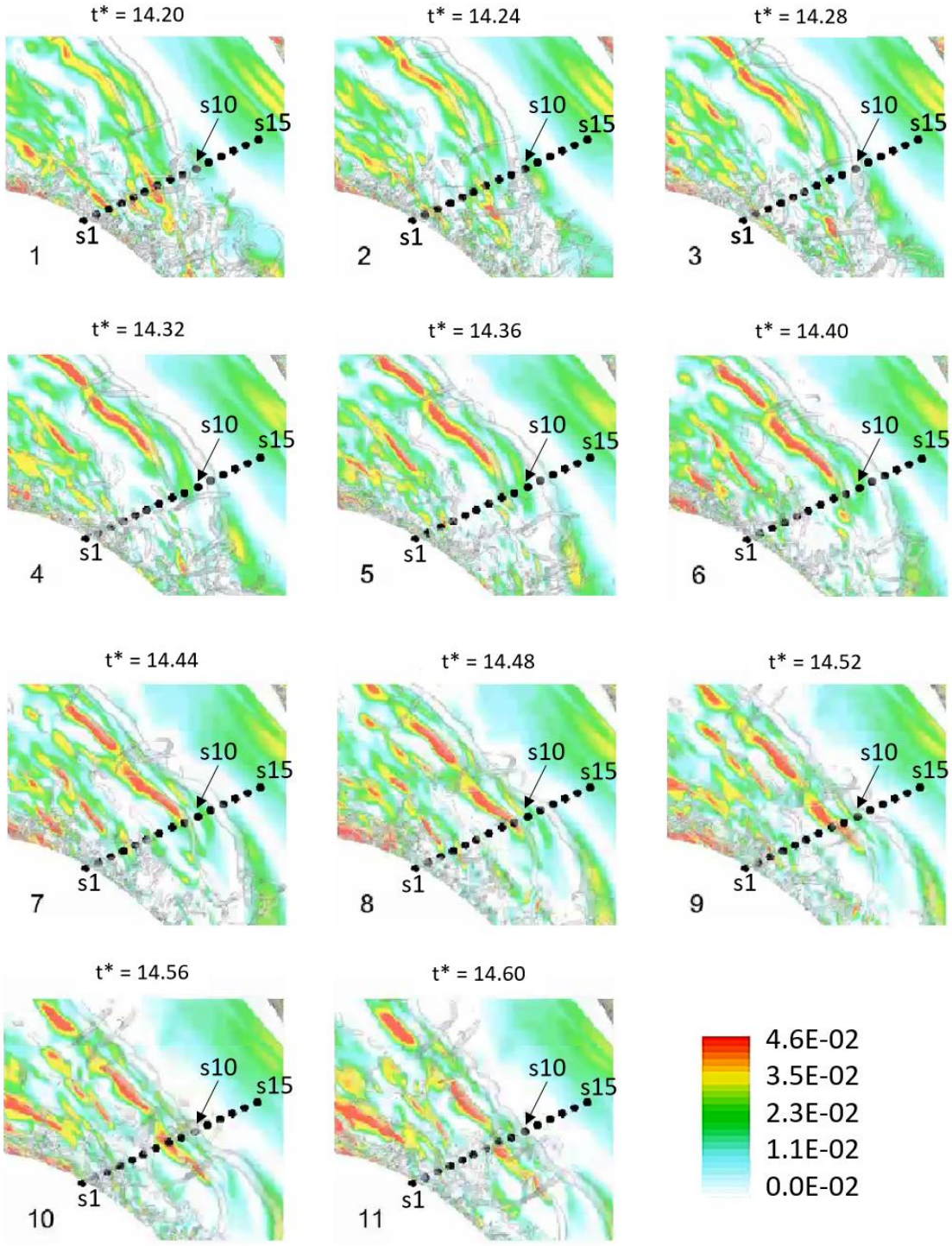

Figure 3-8. Contour plots of skin friction on the endwall and isosurfaces showing the sweep of the PV over s9, s10, and s11.

3.2 Simultaneous Hot-Film Sensors

The positioning of the hot-films was based upon prior measurements of the passage flow structure and the numerical results [Gross et al. 2016, Marks et al. 2016, Gross et al. 2017] which used tunnel conditions A from Table 2-2. Simultaneous measurements from two sets of hot-films are discussed in this section. One set of hot-films probes were placed along the trajectory of the PV from the leading edge to the trailing edge near the suction surface where the PV interacts with the SSCSV. A second set of sensors, array EW4, was mounted in approximately the center of the passage and oriented in the pitchwise direction, normal to the trajectory of the PV. Data from the sensors in EW4 will be used to describe the pitchwise fluctuations of the PV. The naming convention and position of the sensors is discussed in Section 2.3.1, the locations are depicted in Figure 2-6, and are presented in table format in Appendix C.

3.2.1 Pitchwise Array

The five sensors on array EW4, spaced at 5mm, were oriented across the passage normal to the secondary flow direction. The array was positioned so that the centermost sensor, EW4c, was located at the mean center of the PV when under flow condition A. Decreasing the FSTI, a shift in the PV and a change in strength can be expected. Using SPIV results from flow condition B, Figure 3-9 shows the time averaged velocity vectors and Q-criterion measured in a plane aligned with sensor array EW4. In this plane, the separated shear layer rises above the endwall from the PS, the left in Figure 3-9, to the right until rolling up into the PV. The location of the PV under flow condition B was considered close enough to that of flow condition A to not require moving the hot-films. Prior measurements and ILES of the flow through the passage shown by Gross [2017] have described the transient behavior of the PV. The simulation, the results of which are discussed in Section 3.1, helped guide interpretation of the experimental hot-film sensors signals.

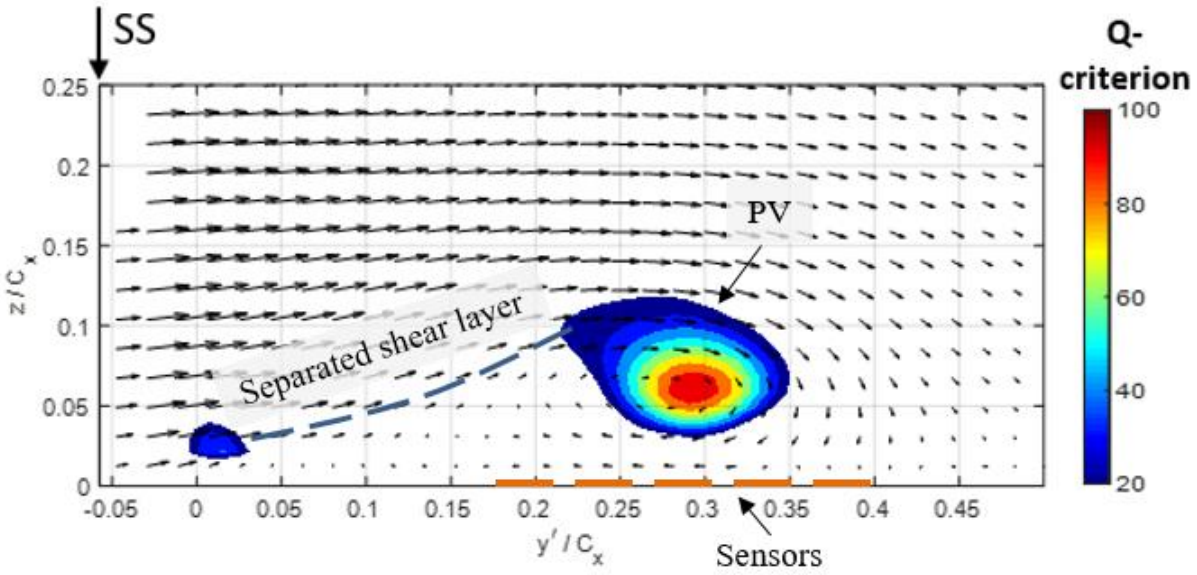

Figure 3-9. Secondary velocity vectors and Q-Criterion in the EW4 plane from SPIV under flow condition B.

Under flow condition A, Figure 3-11 shows the voltage signal fluctuations across the array for a duration of five seconds. The voltage fluctuations are the largest at the center three sensors where the PV has the strongest effect. The frequency spectrum of the signal is plotted in Figure 3-10, showing strong fluctuations in sensors EW4c and EW4d centered around 22Hz. An event occurring at 22Hz corresponds to a non-dimensional time of approximately 3, which is the time the numerical simulation showed as the length of one period of the PV bursting and reforming. This frequency band is not apparent in EW4a and EW4e sensors, but it is discernable from the EW4b thru EWd sensors. The voltage fluctuations are directly related to the heat transfer fluctuation over the sensor. The energy band around 22Hz appears related to downward spikes in the raw voltage signal, as the downward spikes appear every 35ms to 50ms. The spikes in the voltage signal indicate instances in which less heat is transferred, which corresponds to a notable decrease in the near wall

flow. These downward spikes are occasionally evident in the signal from sensor EW4e, but not in the signal of sensor EW4a, which shows that the change in airflow occurs downstream of the PV and not in the upstream separated shear layer side. The cause of these downward spikes is further described in Section 3.3.

Looking at a much zoomed-in snapshot in time of the data in Figure 3-11, Figure 3-12 displays similar fluctuations with a time lag, peaks (1), dips (2&3), and gradually increasing plateaus (4). Even these similar features have irregularities that only correspond with an adjacent sensor, such as the peak at the end of the plateau in sensors EW4b and EW4c, and a drop at the start of the plateau in sensors EW4d and EW4e. The start of the plateaus marked 1 and 4 in trace EW4c occur at a period of roughly 150ms, which corresponds to 6.6Hz. This frequency is at the lowest

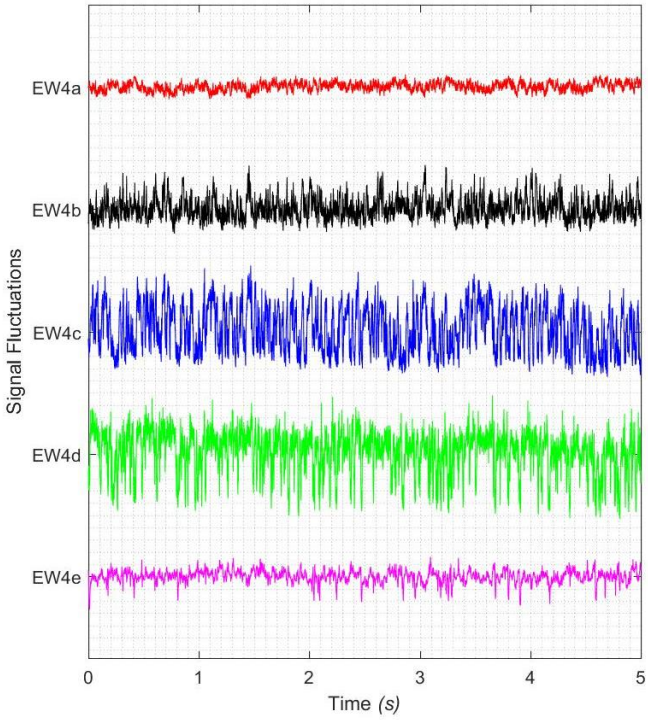

Figure 3-11. Voltage fluctuations across the passage vortex under flow condition A ($\delta_{99\%}$= 9.3%Cx).

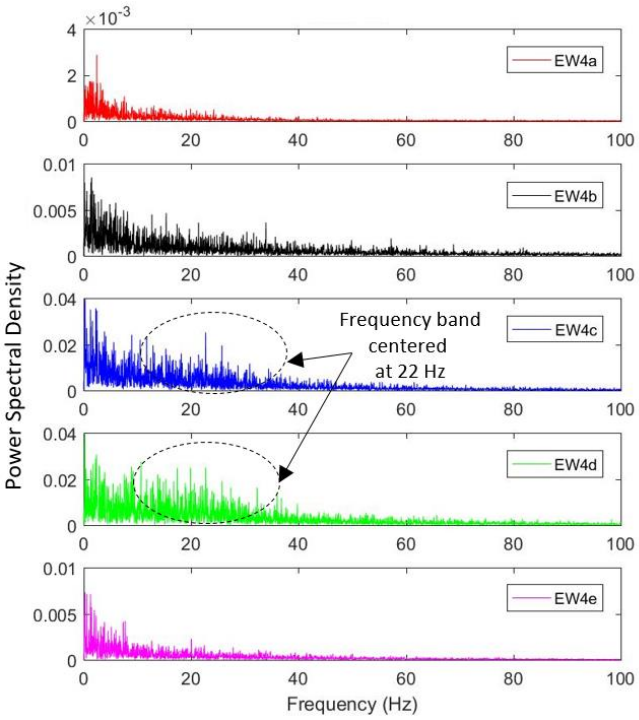

Figure 3-10. Power spectral density frequencies under flow condition A ($\delta_{99\%}$= 9.3%Cx). The passage vortex causes a frequency band centered at 22Hz.

part of the frequency band. The width of the plateaus ranges from 15ms to 35ms. The calmness of a signal from a sensor located slightly upstream of the PV establishes that these reductions in heat transfer are a result of either the PV pitchwise oscillations or sweeping from the pressure surface to the suction surface, or the PV momentarily lifting off the endwall or losing coherence as revealed in the ILES. This loss of coherence was seen using flow

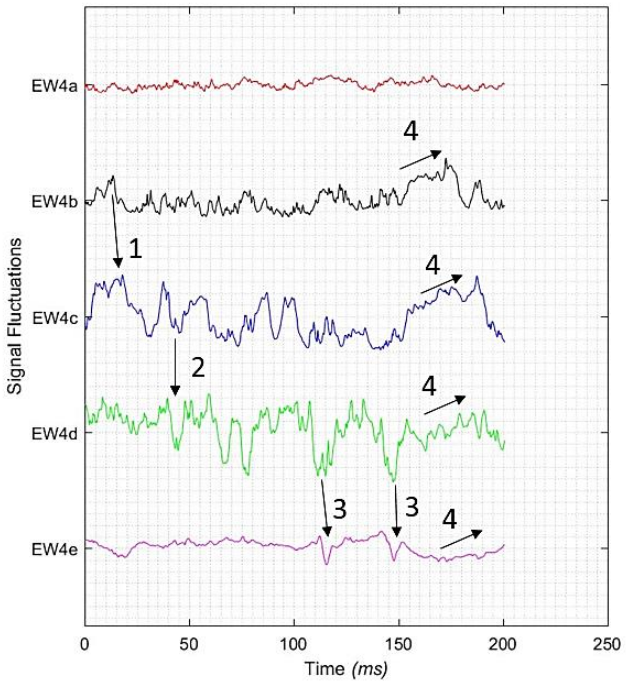

Figure 3-12. Voltage fluctuation in the pitchwise array under flow condition A ($\delta_{99\%}$= 9.3%Cx).

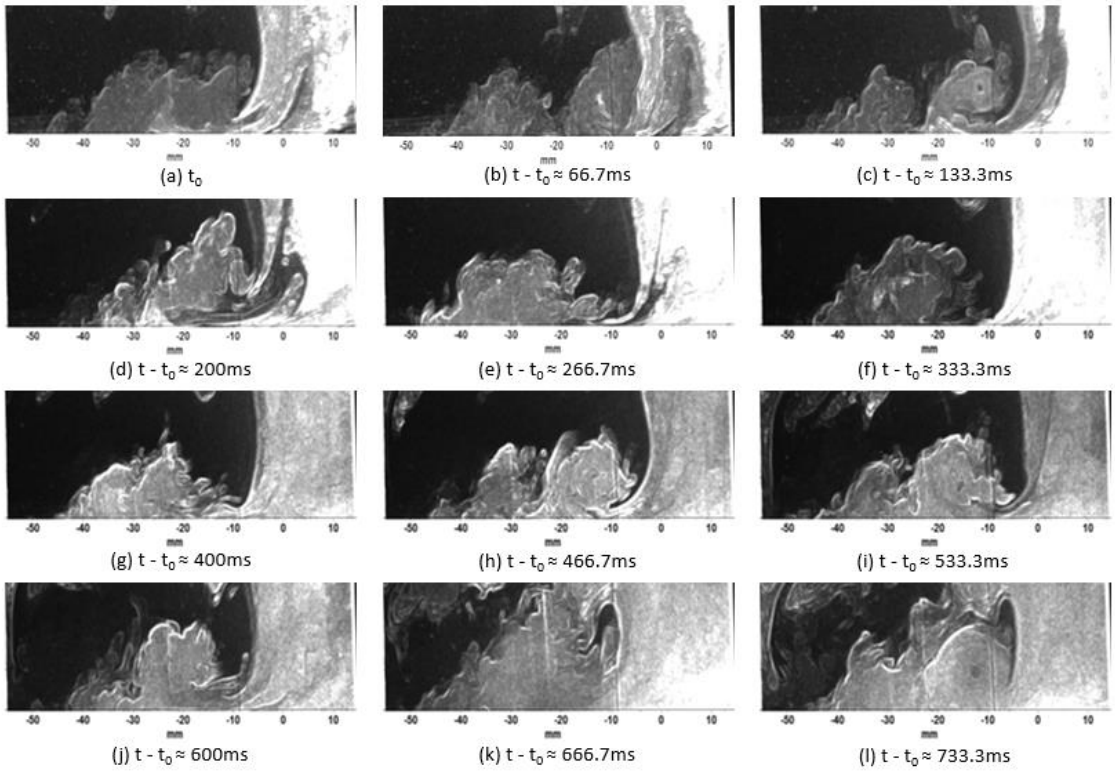

Figure 3-13. Flow visualization snapshots at 15Hz, flow condition B. Two passage vortices form (a-c), disperse (d), create turbulent flow (e-f), reform (g-i), and dissipate to turbulence again (j-k).

visualization as well, see Figure 3-13. The images in Figure 3-13 were created in the same PIV

plane shown in Figure 2-6. Although, the flow visualization images are not time-resolved, they provide a snapshot into different PV realizations, such as a clear coherent PV (Figure 3-13 a-c, g-i, l), the dissolving of the PV (Figure 3-13 d, j-k), and the solely turbulence regime (Figure 3-13 e-f). In some cases, most notably downstream in the passage, vortical tendrils wrap themselves around the PV prior to it losing coherence.

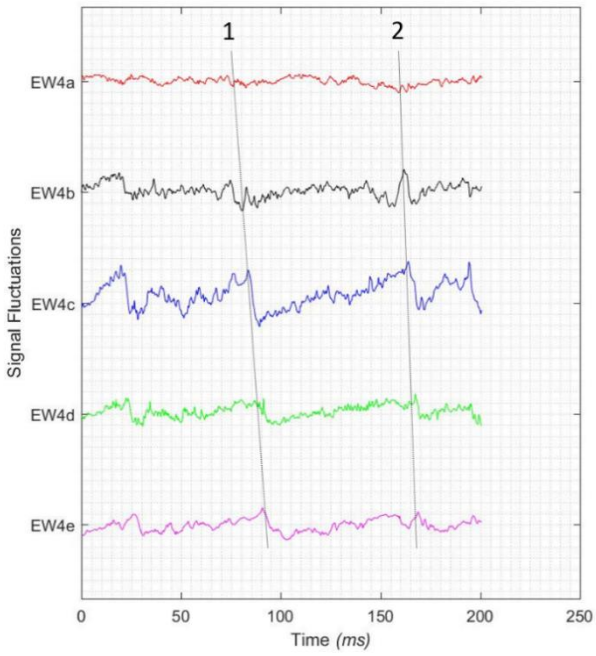

Figure 3-14. Voltage fluctuations across the passage vortex under flow condition B ($\delta_{99\%}$ = 7.3%Cx).

Under flow condition B, which has the lower FSTI, the PV signal weakens but expands in space. The lack of significant downward voltage spikes in Figure 3-14 indicate that the heat transfer does not change as dramatically as under flow condition A. However, all five sensors in array EW4 now pick up the PV frequency band, Figure 3-15. Although the 22Hz frequency is still present, the strongest frequency signals are between 10Hz and 15Hz which corresponds to periods of 66ms and 100ms. These times are the time frame between the events 1 and 2 in Figure 3-14. The weaker raw voltage signal and the

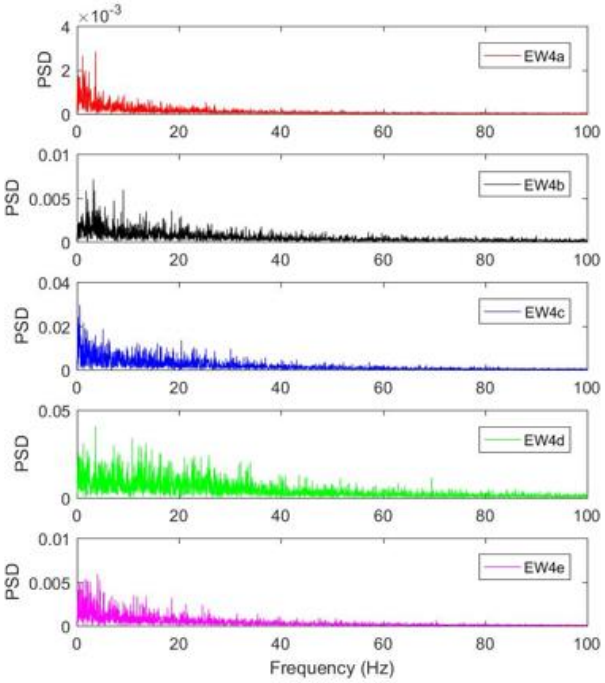

Figure 3-15. Power spectral density frequencies under flow condition B (δ99%= 7.5%Cx).

extended spacing between sensors picking up the PV signal indicate that the PV is wider as earlier established by SPIV, Figure 3-9. Research on FSTI effects on blunt body flows shows that with an increase in FSTI the vortex core shifts closer to the blunt body [Lange et al. 2018]. In the turbine passage, the decrease in FSTI could account for the widening effect on the PV.

Under flow condition C (low FSTI), a much thinner boundary layer forms. Both the SPIV, Figure 3-16, and the raw voltage trace, Figure 3-17, show that the PV shrinks in size and moves towards the pressure surface. The frequency spectrum (Figure 3-18) of the voltage trace (Figure 3-17) is similar to previous power spectral density plots. The frequency spectrum shows that the PV still has fluctuations which create a band of frequencies centered around 22Hz, although the

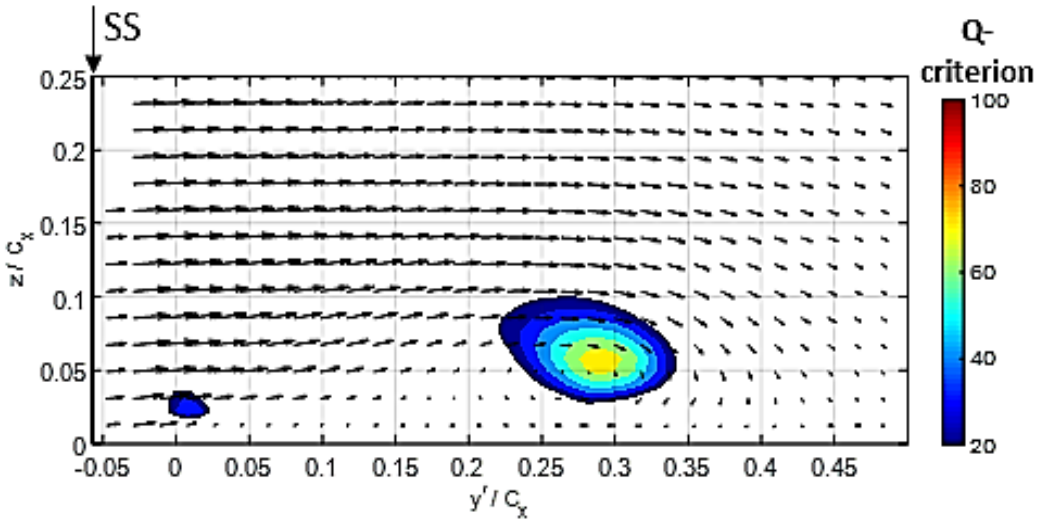

Figure 3-16. The time-average passage vortex decreases in size and shifts locations with a decrease in BL thickness, flow condition C.

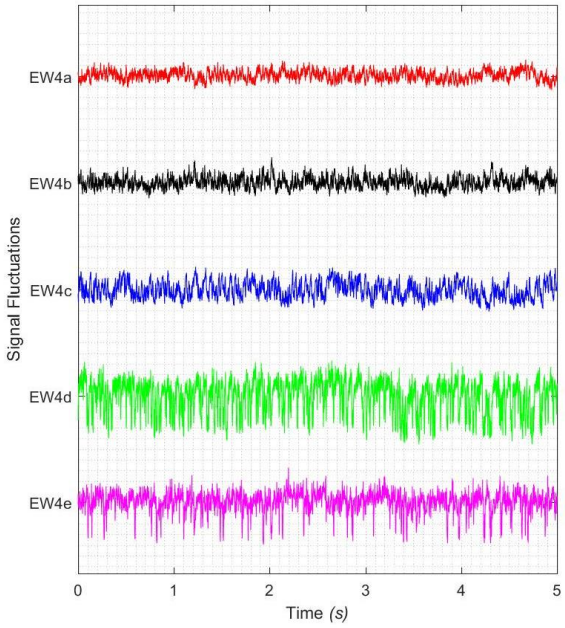

Figure 3-17. Voltage fluctuations across the passage vortex under flow condition C (δ99%= 2.5%Cx).

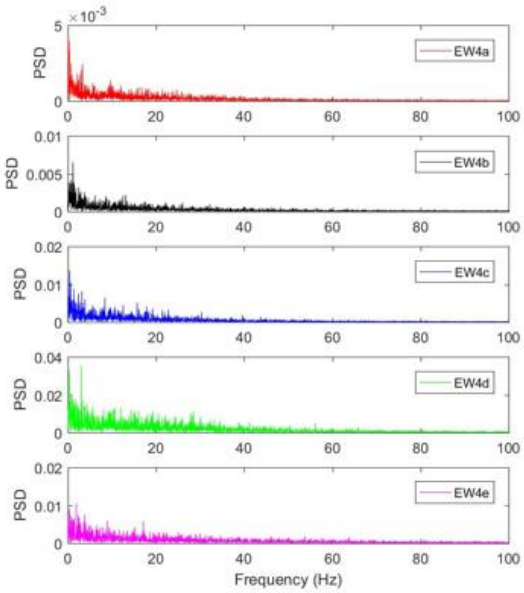

Figure 3-18. Power spectral density frequencies under flow condition C (δ99%= 2.5%Cx).

upper frequencies in the band have dissipated and the magnitudes have declined. This implies that the frequency of the PV is mostly independent of FSTI and boundary layer thickness, although less apparent under lower FSTI and thinner BL conditions.

3.2.2 Streamwise and Suction Surface Sensors

The PV develops from the pressure side leg of the horseshoe vortex, follows the pressure gradient downstream and across the passages towards the suction surface, and interacts with suction surface flow structures.

Flow condition A generated several interesting results in the streamwise direction. First, Sensor EW2a was situated closest to the leading edge at 5mm. It measured a very different signal than sensor EW2b which was positioned 10mm from the leading edge and 5mm from sensor EW2a. EW2b also shows larger fluctuations than the incoming boundary layer which was measured with the sensor EW1a. This increase in turbulence between the EW1 sensor and the EW2 array was

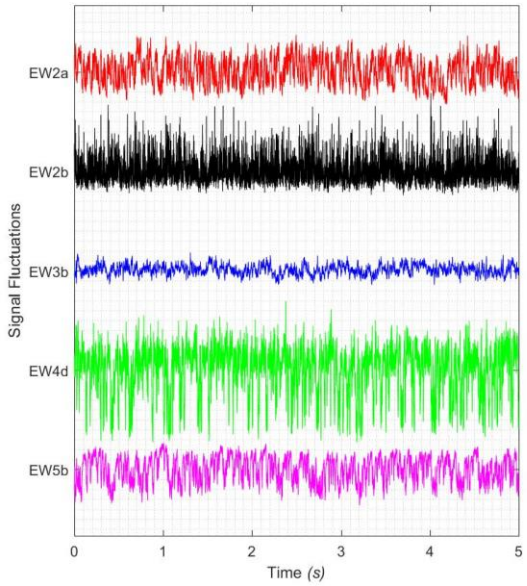

Figure 3-19. Voltage fluctuations through the passage under flow condition A (δ99%= 9.3%Cx).

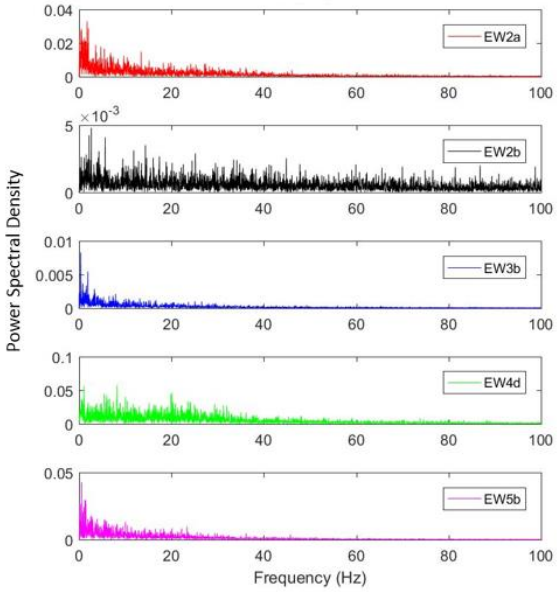

Figure 3-20. Power spectral density frequencies through the passage under flow condition A (δ99%= 9.3%Cx).

expected for two reasons: the incoming boundary layer had another axial chord length to develop, and the development of the tip of the horseshoe vortex upstream of the leading edge as seen in smoke visualization [Wang 1997], the ILES [Gross 2016], and other experiments [Praisner2006].

The magnitude of fluctuations at sensor EW3b were lower than the other sensors. This is most likely due to the positioning of array EW3 just upstream of the PV. Sensors EW4d and EW5b show the signature of the passage vortex, with magnitude fluctuations at EW5b smaller than EW4d. The raw data trace and the frequency of sensor EW5b are very similar in size and shape to those of EW2a, Figure 3-19 and Figure 3-20. Similar features, such as dips (1&2) and increases (3) in voltage, can be seen propagating from EW2a to EW4b and EW5b,

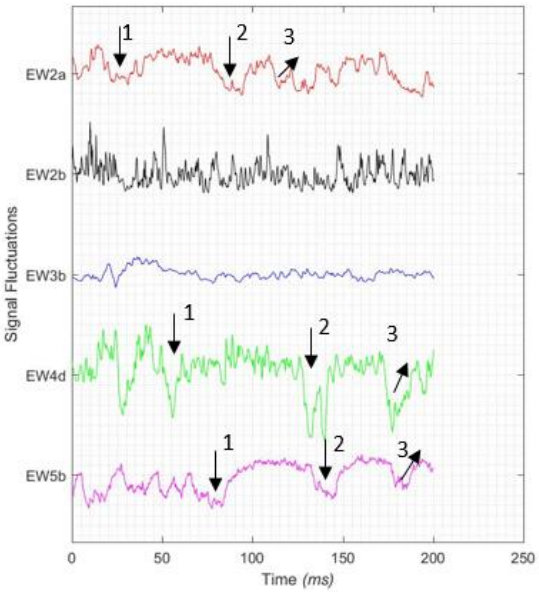

Figure 3-21. Voltage fluctuation events propagating through the passage under flow condition A (δ99% = 9.3%Cx). Events propagate from the leading edge (EW2a) through the passage vortex (EW4d and EW5b), as shown by dips in the voltage (1) and (2) and also rises (3).

as seen in Figure 3-21. The dips occur every 50ms to 100ms, which corresponds to 10Hz to 20Hz, the frequencies of major peaks in the FFT.

As previously stated, the boundary layer characteristics of flow condition A were matched in the ILES, but not the elevated FSTI. Several numerical probes were placed in similar regions as EW1, EW2, EW3, and EW5; however, the probes in the numerical simulation were offset from the endwall. As discussed in Appendix B, the discrepancy in location can significantly change the signal. For example, the numerical simulation shows a large peak in the frequency domain, Figure 3-4, at the leading edge which corresponds to sensors in the array EW2, neither of which exhibited the peak. Nonetheless, it was found that although both hot-film sensors EW2a and EW2b are on the endwall and only 5mm separate them, they show considerably different signals because the flow changes and shifts drastically at the tip of the leading edge. The frequency that is found numerically for upstream of the passage (not shown) is very flat and consistent across all frequencies, which agrees with the experimental data obtained with sensor EW1a (not shown). Figure 3-4 shows that the peak normalized frequencies for the probes around the PV are less than 0.5 and are centered at 0.35 which correspond to 35Hz and 22Hz respectively. This is consistent with what the band centered around 22Hz from the experimental data found to be the frequency of the PV.

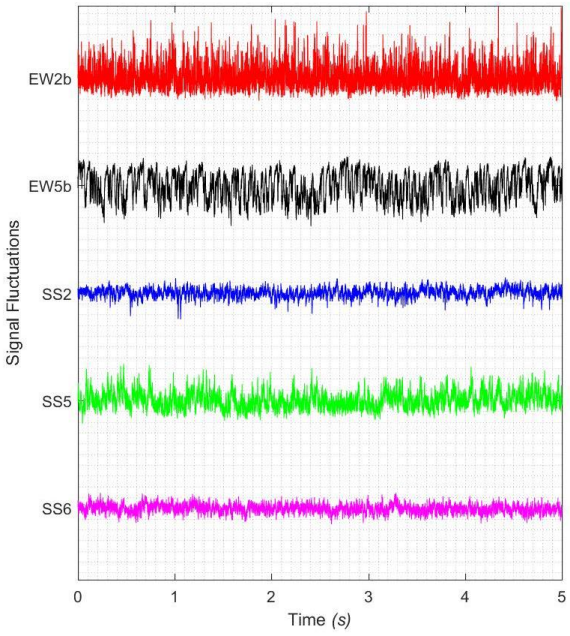

Figure 3-22. Voltage fluctuations on the suctions surface and near the passage vortex under flow condition A (δ99% = 9.3%Cx).

The PV interacts with the suction surface flow structures. There is a 2D loss region above this interaction, where several sensors were positioned. This 2D region includes a separation bubble that

reattaches. Reattachment occurs by the time the flow reaches SS2, Figure 3-22. Sensor SS6 has a similar signal and frequency domain, Figure 3-23, indication that SS6 is in the 2D region despite being closer to the endwall. Sensor SS5, however, has a more turbulent raw voltage trace and more frequency peaks in the 22Hz band associated with the PV which can be seen in sensor EW5b. Overall, it was determined that more sensors would be needed on the SS to get a better understanding of its flow field.

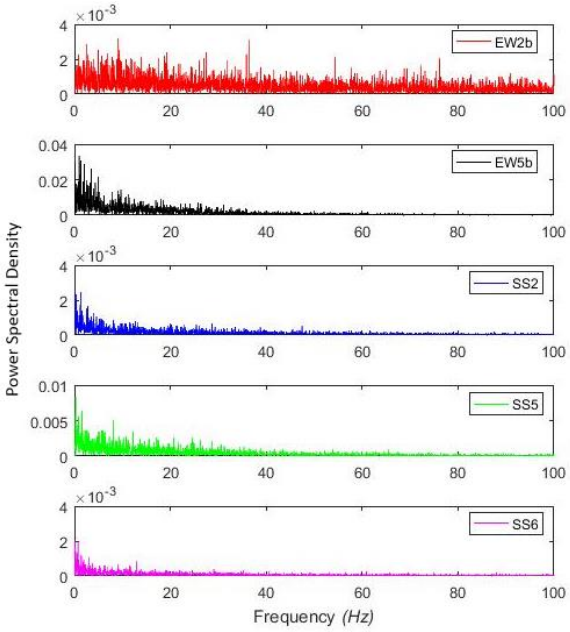

Figure 3-23. Power spectral density frequencies on the suctions surface and in the passage vortex under flow condition A (δ99%= 9.3%Cx).

Flow condition B (low FSTI) has a reduced turbulent incoming flow, which is picked up by sensors EW1a (not shown), EW2a and EW3b, Figure 3-24. The PV affects EW5b just as strongly as it affects EW4c, not shown; however, the intensity of the fluctuations is not as dramatic as those seen from the PV under the higher FSTI. The boundary layer is notably thinner under flow condition B. Consequently, sensor SS5 is above the PV interaction with the suction surface and is in the turbulent reattachment section of the 2D loss region.

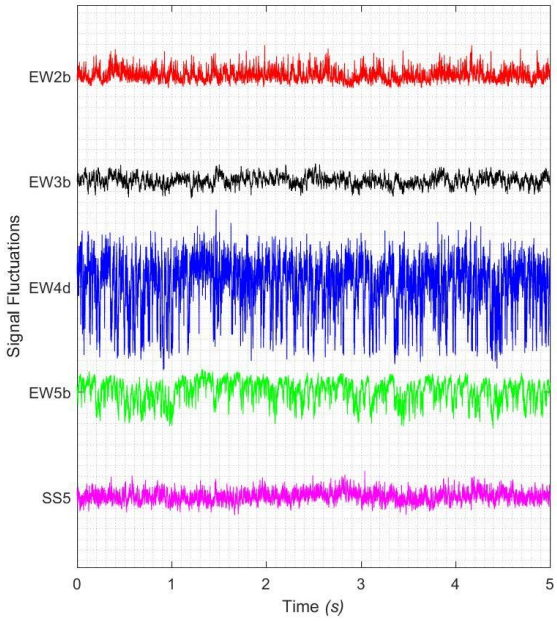

Figure 3-24. Voltage fluctuations through the passage and on the suction surface under flow condition B (δ99%= 7.5%Cx).

Under flow Condition C, the sensors EW1a, EW2a, EW2b, and EW3b also observe a lower turbulence in the incoming flow, Figure 3-25. The raw signals of sensors EW4c and

EW5b are very similar to what they were under flow condition B. The similarities indicated EW5b is also experiencing effects from the PV, which appears weaker in this flow condition.

3.2.3 Discussion of Bimodal Behavior and Passage Vortex Bursting

Gross et al. [2017] propose that the bimodal behavior of the horseshoe vortex is responsible for the observed intermittent loss of coherence of the PV. The ILES velocity signal at the four regions of the endwall were plotted versus non-dimensionalized time in Figure 3-3. The time lag of similar disturbance events propagating between sensor positions are highlighted with an orange arrow. It takes a non-dimensional time of roughly t* = 1 to 1.5 (15.5ms to 23ms) for disturbances to propagate from the leading edge (EW2) through the passage (EW5). The experimental hot-film signal in the same locations for flow conditions A and B are plotted in Figure 3-21 and Figure 3-26 respectively. Similar events are highlighted in the figures labeled (2). The time lag between EW2a and EW4c is roughly 45ms with an additional lag of 5ms to reach EW5b. Similar disturbances with a time lag are shown in the experiments regardless of FSTI level. This finding

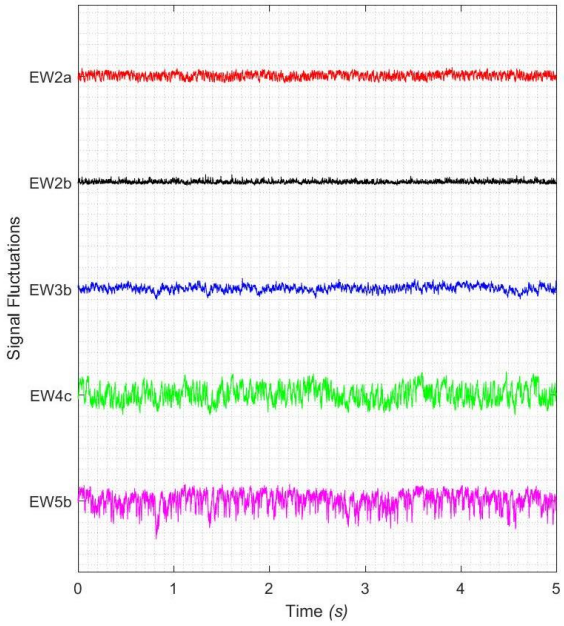

Figure 3-25. Voltage fluctuations through the passage under flow condition C (δ99%= 2.5%Cx).

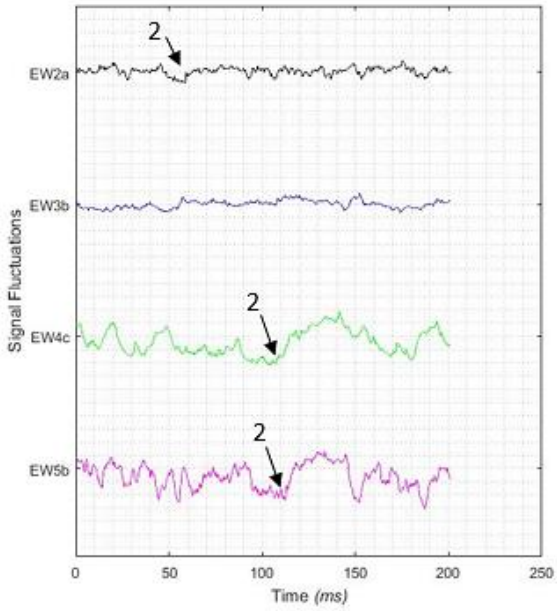

Figure 3-26. Raw signal trace in flow condition B (δ99%= 7.5%Cx).

lends support to the argument in Gross et al. [2017] that the bimodal behavior of the horseshoe structure is related to the loss of coherence in the PV.

3.3 Concurrent Hot-Film and Flow Visualization

For the concurrent hot-film data acquisition and flow visualization, eight hot-films were positioned in the EW4 region named EW4a thorough EW4h. The positions are specified in Appendix C.2. The centers of the platinum of the sensors were positioned 18mm downstream of the laser plane. This was done to allow the laser plane to stay in the previously used location, from Section 3.2, when run concurrently with the hot-films. Therefore, the flow visualization was acquired in a plane parallel to but offset from the hot-film array, 18mm upstream from the center of the platinum sensors. This gave the copper leads approximately 14mm of clearance from the laser sheet.

The hot-films were operated at 15kHz with a low-pass hardware filter of 5kHz and a high-pass hardware filter of 0.1Hz. The high-repetition rate SPIV was obtained at 2.5kHz using double frames with a *dt* of 10μs, and the high-repetition rate flow-visualization was obtained at 5kHz. For both techniques, 5300 images were acquired resulting in 2.12s and 1.06s of data for the SPIV and flow-visualization, respectively. The specific details of the SPIV system and method of aligning the hot-film signal are detailed in Section 2.3.2.

One of the main goals was to connect the hot-film signal signatures with real flow events. The first was to find a flow phenomenon to explain the large dip in the signal, and the other was to find a signature that could indicate a bursting event. The numerical simulation, discussed in Section 3.1, gives the expectation that the rise after a dip in the signal should be caused by the pitchwise sweeping motion of the PV.

The hot-films EW4a through EW4h are at the same locations as the numerical probes s4 through s11; however, the signals obtained by the hot-films at the high FSTI were more similar to the signals of probes s6 through s13. This is due to the small difference in the separation length and

PV between the experimental and the simulation. Figure 3-27 shows the raw hot-film signal under flow condition A. The signals from EW4e through EW4h have downward spikes like those seen in Section 3.2.1. When the FSTI is lowered, the PV shifts toward the PS. In Figure 3-28, the downward spikes are concentrated on the EW4g and EW4h sensors.

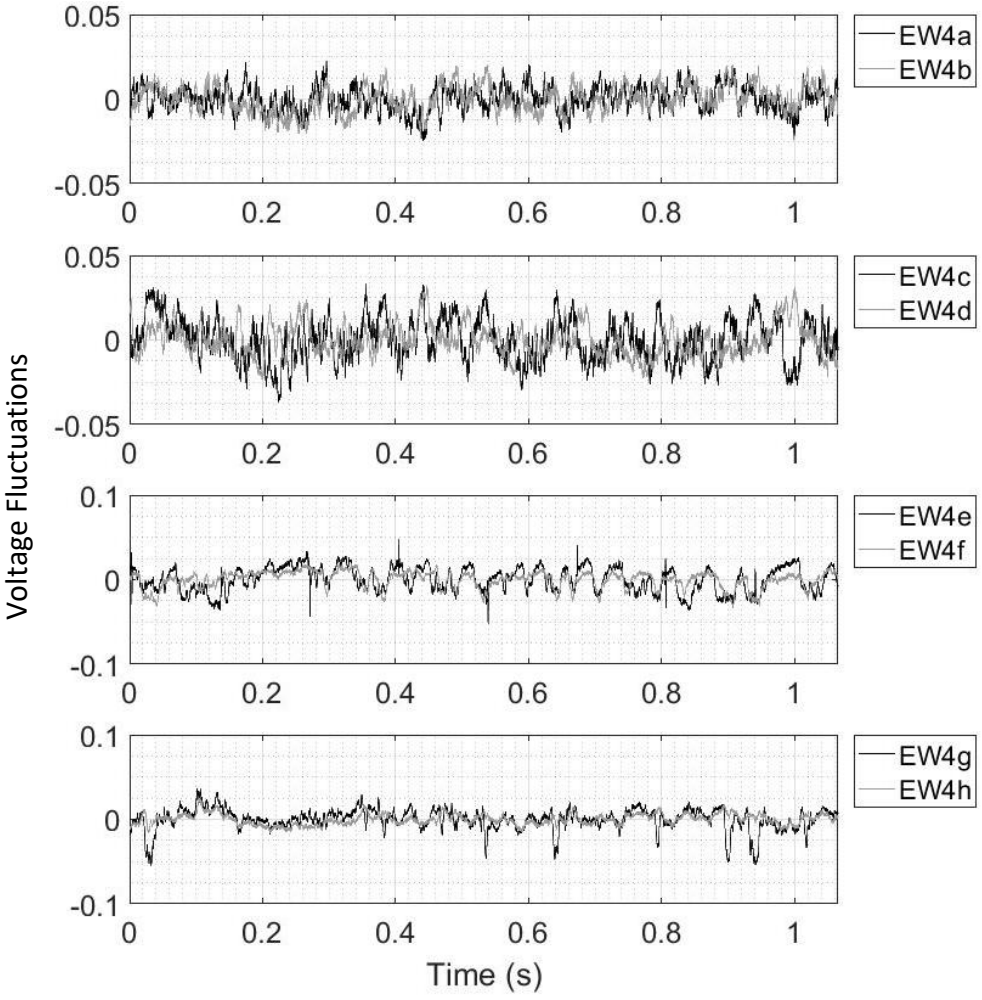

Figure 3-27. Hot-film signal during flow-visualization under flow condition A (high FSTI).

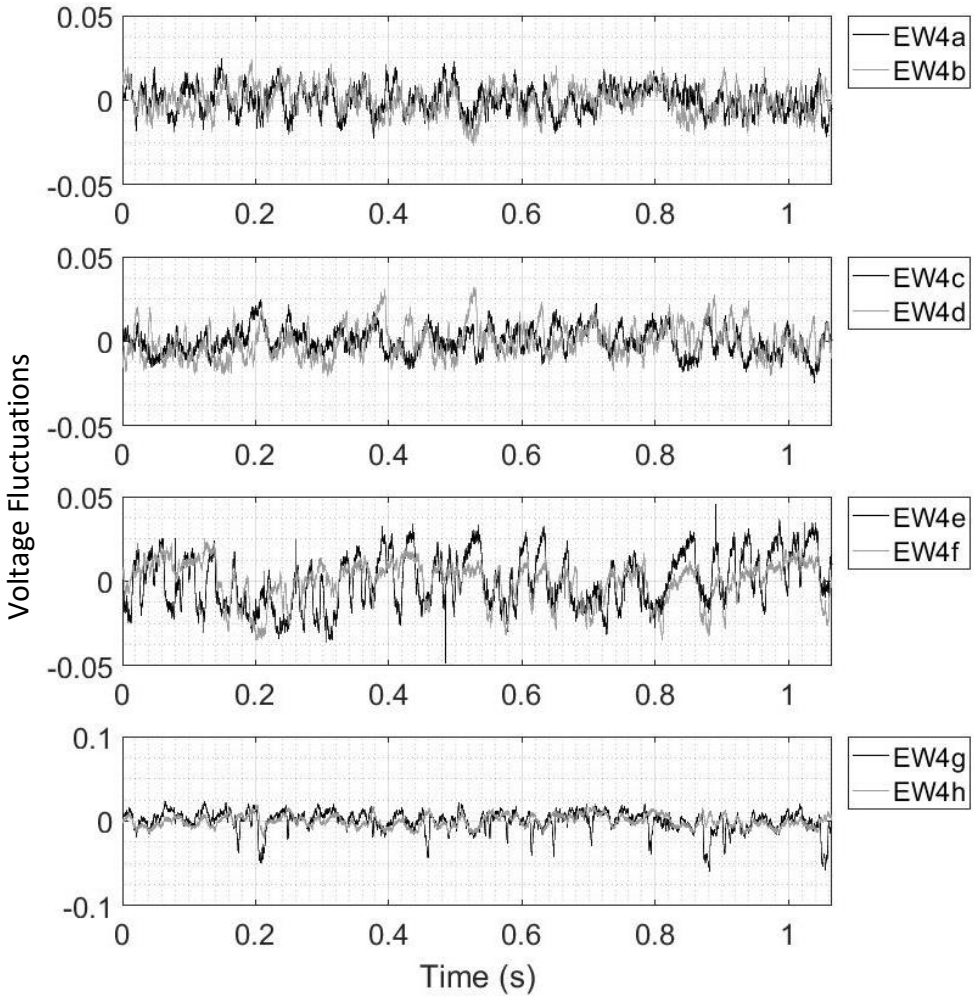

Figure 3-28. Hot-film signal during flow-visualization under flow condition B (low FSTI).

The FFTs of these signals provide comparable results to those in Section 3.2. Both signals have the frequency band around 22Hz that was previously seen in Section 3.2. Interestingly, under flow condition B (low FST/i), EW4a and EW4h have a peak at 57Hz. This frequency correspond to a time of 17.5ms, which is approximately the convective time through the passage based on the suction side length and the average velocity through the passage. EW4c shows a similar peak under flow condition A. This is consistent with the 10mm (distance of two sensor) shift of the PV. Strong peaks are also still occurring at 19Hz and 32Hz or 52ms and 31ms respectively. 32Hz corresponds to f^*=0.5, which makes the corresponding time half of the convective time through the passage.

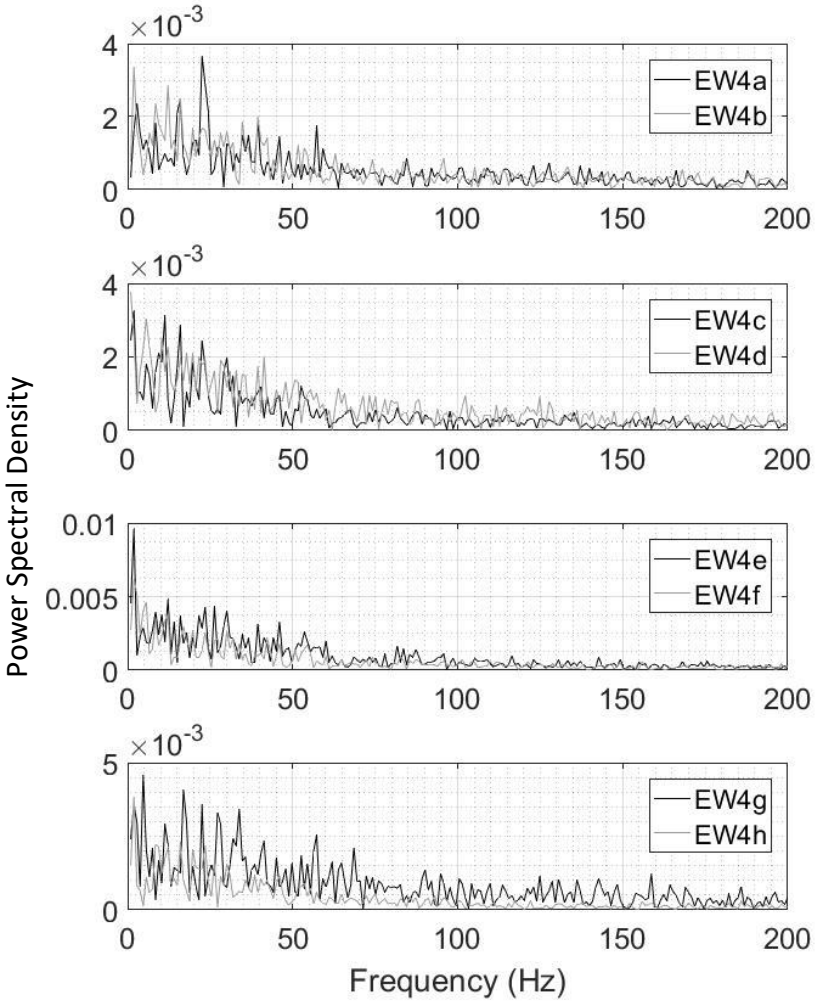

Figure 3-29. FFT of the signal in Figure 3-28, flow condition B (low FSTI).

Figure 3-31 shows the hot-film voltage signal of three hot-film sensors and four corresponding flow-visualization images. At time 587.1ms, the PV is weakening. There is a dip in the signals EW4d and EW4e, indicating the SS of the PV. At time 590.9ms, the PV bursts, which starts an increase in the voltage. At time 597.1ms, the PV reforms and the voltage does not increase as rapidly. By time 606.4ms, the PV has reformed and has swept across EW4d twice.

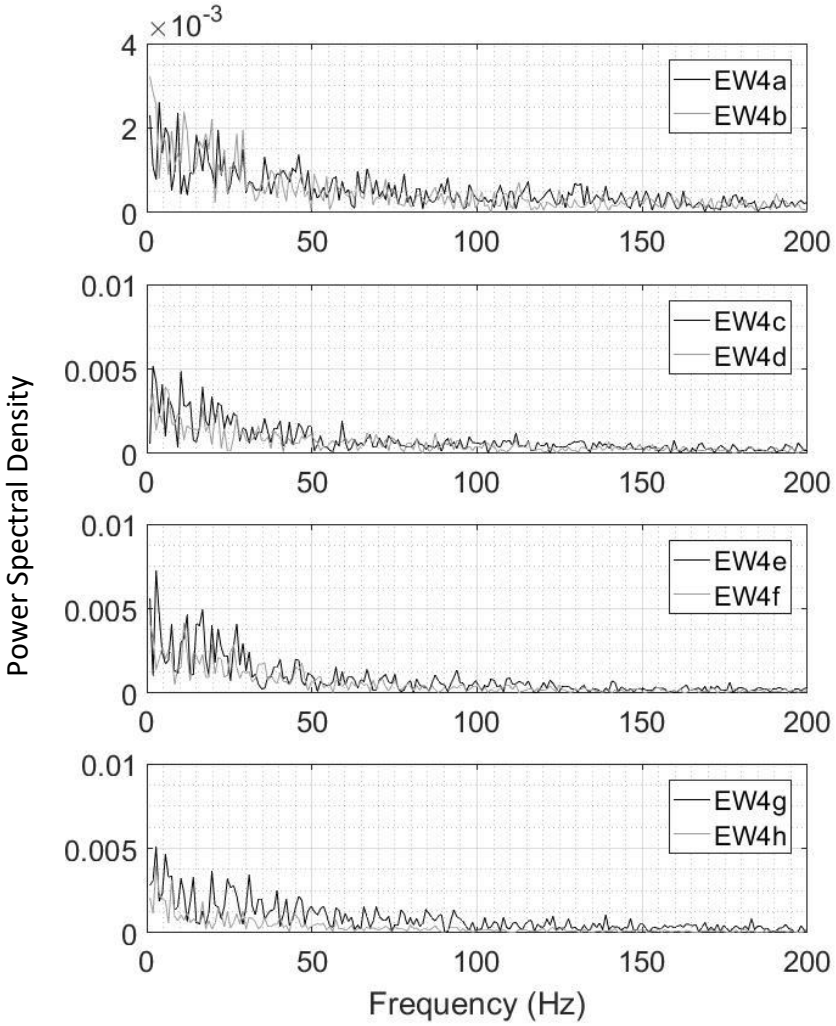

Figure 3-30. FFT of the signal in Figure 3-27, flow condition A (high FSTI).

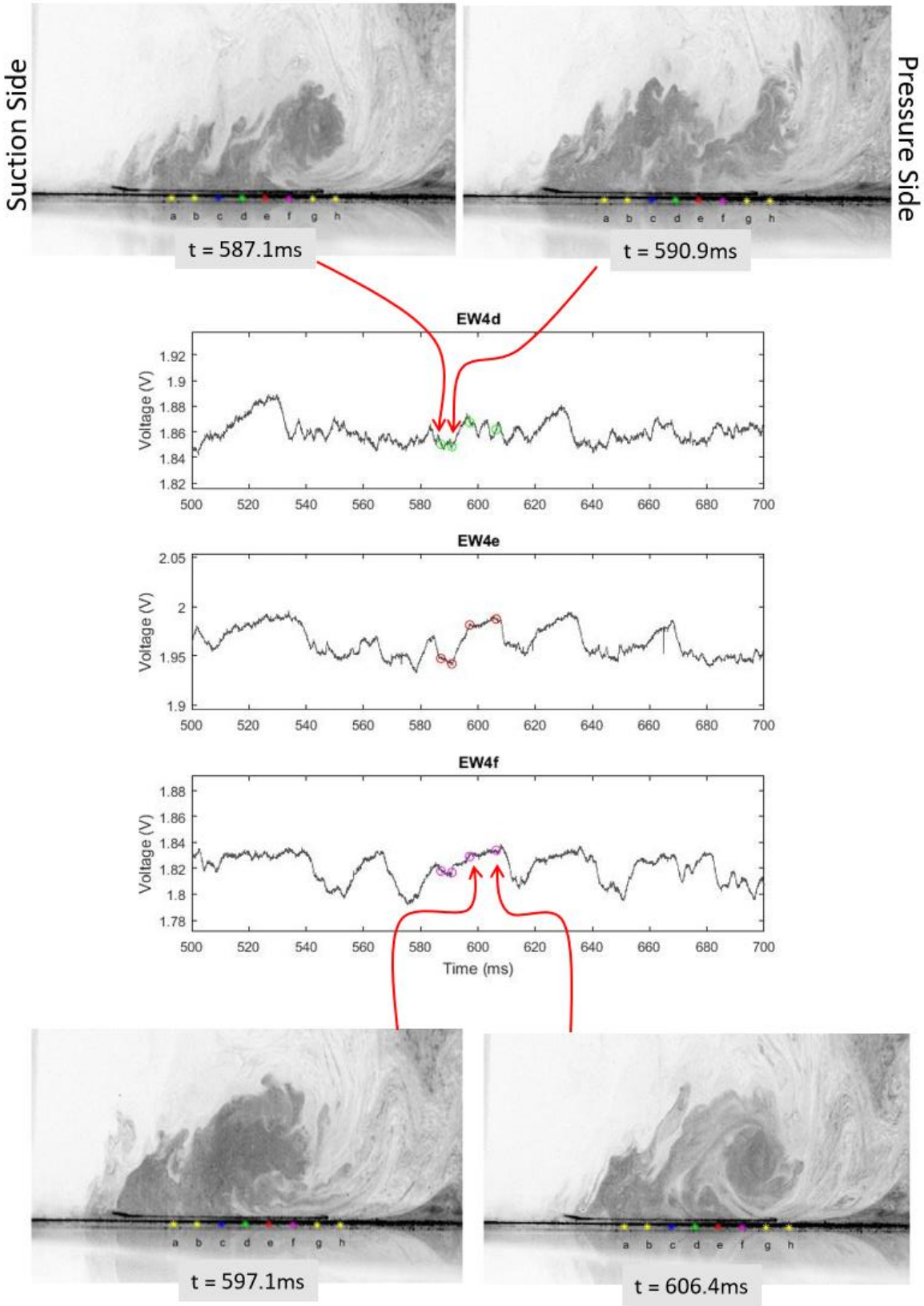

Figure 3-31. Hot-film signal and flow-visualization through a bursting event under flow condition B (low FSTI).

The dips in the signals are caused by the PV liftoff which occurs on its suction side, Figure 3-32. This decrease in heat transfer at the liftoff point was described by Praisner and Smith (2006) when looking at the saddle point of a horseshoe vortex. A notable feature that occurs near the liftoff point is a secondary vortex. This secondary vortex is a result of the PV pulling the cross-flow off the endwall, thereby creating a counter-rotating secondary-flow feature. This flow feature instigates the large dips in the hot-film signals. These dips can therefore be used to calculate the pitchwise sweep of the PV. For example, in Figure 3-12, the dips labeled 2 and 3 are the PV sweeping across the sensors. EW4e is nearest the PS in the figure, with the only real variation in the signal being the dips labeled 3, indicating that at those times the PV got close to the PS. Only a very strong PV to approach the pressure surface.

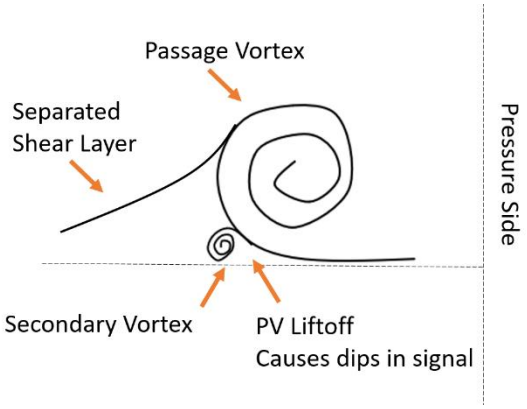

Figure 3-32. PV gets fed by the PS and the cross-flow. The PV lifts up off the surface causing a secondary vortex to form and producing most of the dips in the hot-film signals.

The bursting event is the result of several flow phenomena. Figure 3-33 is a schematic of the steps the flow proceeds though surronding a bursting event. The bursting event generally starts with a strong PV near the PS (A), however this step may be skipped if two bursting events occur within a short timespan. The PV then weakens and moves closer to the SS and the endwall (B). Then the PV looses coherence, or bursts (C). The vortex core disappears and the flow takes on the appearance of general turbulent flow. Next, the smaller vortices that were within the separated shear layer become larger and new small vortices form (D). Finally, a redeveloped PV appears (E).

While the PV has lost coherence, there is no PV liftoff to create the dips in the hot-film signal. Consequently, no dips in the signal occur across the hot-films that normally exhibit dips, is a good indication that a burst has occurred. Another way to describe a signal with no dips would be a plateau. Subsequently, the plateau labeled 4 in Figure 3-12 can be assumed to be a bursting

event. Looking at Figure 3-27, it can be determined that a bursting event occurs around 0.3s and another around 0.38s. At these times, the hot-films EW4d, EW4e, and EW4f have the signature

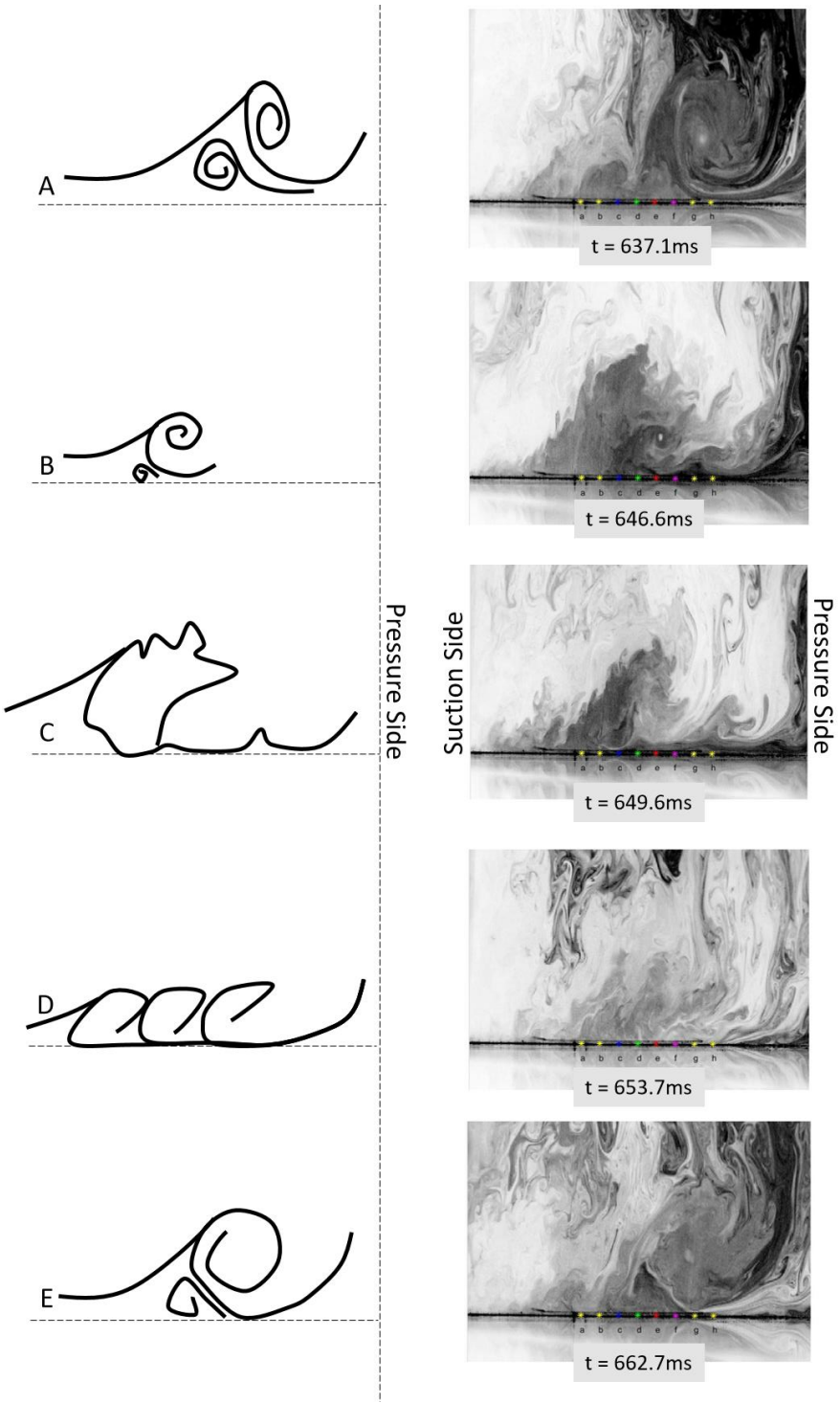

Figure 3-33. Left: Schematic of steps in a bursting event (A) a strong PV near PS, (B) a weaker PV further from the PS, (C) the PV loses coherence (bursts), (D) several weak vortices form, and (E) the PV reforms. Right: Associated flow-visualization under flow condition B (high FSTI).

determined to indicate a bursting event. Similarly, at the low FSTI level, Figure 3-28, in the time frame of 0.58s to 0.64s, the PV is seen to be very strong, sweeping across EW4g several times.

The hot-film signals shown in Figure 3-34 correspond with the flow-visualization images in Figure 3-33. At time 637.1ms, there is a strong PV near the PS. At 646.6ms, this PV has

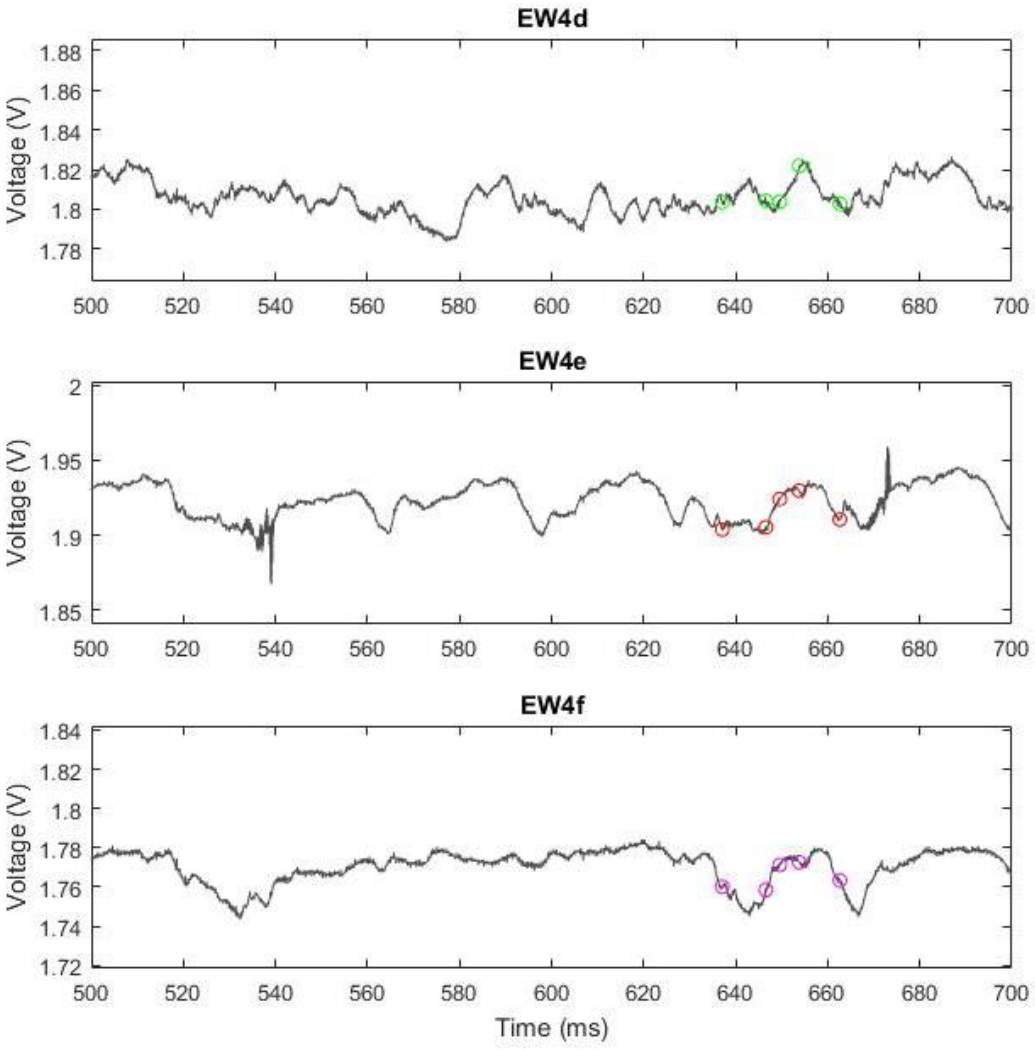

Figure 3-34. Hot-film signal corresponding to flow-visualization images in Figure 3-33, flow condition A (high FSTI). Each circled data point is the time of one of the images.

weakened, consequently moving away from the PS and nearer the endwall. The voltage signal is about to climb across all three signals, indicating a burst. At 649.6ms, the PV has lost coherence, seen in the change in slope of the EW4d signal. At 653.7ms, small vortices have formed. And by

662.7ms the PV has reformed. In the signal in Figure 3-34 another burst occurs at approximately 668ms, which does not allow the PV to regain as much strength as it had at time 637.1ms.

The bursting events are stochastic. They can have a in fast recurrence, with only 25ms separating events, which would put the frequency of bursting at approximately 40Hz; or it can take 55ms between bursting events, putting the frequency at 18Hz. This would explain the wide frequency band centered around 22Hz.

4. Conclusions

4.1 Simultaneous Hot-Film

The simultaneous hot-film experiment used surface-mounted constant-temperature hot-films to obtain time-resolved data from the flow structures, especially the passage vortex, through the front-loaded low-pressure turbine passage that was subjected to three different incoming boundary layers. Sensors were positioned both in the streamwise and pitchwise directions. It was found that the passage vortex gave a signal with a frequency band centered at 22Hz, which assented with the numerical simulation. The signal across several sensors also detected the signature of the passage vortex and the breadth of its range. The signal events clearly propagate from the leading edge through the passage, although the time between events in the signal expands as it transmits down the passage. The frequency content became stronger at a lower frequency range with the decrease in freestream turbulence intensity and the position will change with a decrease in boundary layer thickness. Regardless of freestream turbulence intensity, the time lag between the leading edge sensor and the downstream sensor lends support to the argument of Gross et al. [2017] that the bimodal behavior of the horseshoe structure is related to the loss of coherence in the PV.

4.2 Concurrent Hot-Film and Flow Visualization

Using hot-films in conjunction with flow-visualization allowed for an increase in the understanding of the transient behavior of the passage vortex. The combination of the two measurement types allowed for identification of particular signatures in the hot-film signal for specific flow phenomena. It was found that the secondary vortex on the suction side of the passage votex is responsible for dips in the hot-film signal; accordingly, the suction side of the passage

vortex can be traced as the passage vortex sweeps across the pitch. It was also found that these dips in the signals are often absent immediately after the passage vortex bursts, creating plateaus across the signals. During a bursting event, the passage vortex weakens and moves toward the suction side, where it loses the clear vortex core (bursts). Next the flow is purely an extension of the turbulent incoming shear layer, until the passage vortex reforms. The bursting event occurs quasiperiodically at rates between 15Hz and 40Hz, which links to the low frequency band centered around 22Hz in the previous experiments.

4.3 Future Work

The hot-film capability developed for the LSWT Facility can be utilized in several ways. The first would be a continuation on the study of the PV. It would be beneficial to look at the PV further upstream in the passage, where there are less influences from the suction surface, possibly the EW3 region from the simultaneous hot-film study. It would also be beneficial to view the hot-films and flow visualization at the leading edge. This, however, will require a redesign of the test section obtain optical access. Another thing that would benefit data acquisition would be installing a DAQ card that is capable of reading the signal from the PTU to the cameras, to perfectly synchronize the hot-film and PIV data in time. Ideally, this would result in an understanding of what causes the PV to lose coherence, which in turn reduces the total passage pressure loss, making the system more efficient with forcing the PV to the burst condition.

The hot-films could also be used in conjunction with other experiments in the cascade tunnel. One of which would be phase locking the hot-films signal with endwall blowing or an upstream wake generator. The hot-films could give an extra piece of information on how the flow features change with the introduction of these and other alterations in flow conditions.

A. Hot-Film Development

A.1 Background

The hot-film sensors used to measure fluctuations in shear stress had to be adapted from their original purpose of measuring heat-flux. As heat-flux gauges, the sensors were double sided and run on a low constant current with measurements ofn the change in resistance. As surface-mounted hot-films, only the air-side of the sensors was used. Instead of using constant current and reading the resistance of the sensors, the hot-films were operated with a TSI IFA 300 Constant Temperature Anemometer (CTA). The CTA uses a Wheatstone bridge and amplifier to adjust the voltage supplied to a hot-film sensor (IFA 300 Manual 2010). As air flows over the sensor, heat is removed reducing the temperature of the sensor, thus decreasing the resistance. By changing the voltage supplied, the CTA keeps the resistance and consequently the temperature of the hot-film constant. The fluctuations in voltage are what is measured and, in anemometry, is correlated to velocity, but in the hot-film application is used to infer the fluctuations in shear stress. An FFT of the voltage signal provides information about the frequency at which signal signatures appear.

The hot-films are designed to be mounted flush to a surface. The hot-films are thin, approximately 0.05mm thick, and flexible. The platinum sensor, thickness of ~800Å, has significantly wider copper leads, Figure A-1.

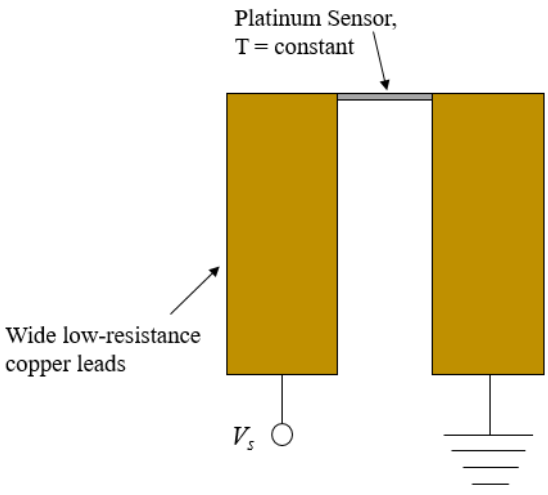

Figure A-1. Schematic of a hot-film sensor.

The leads are much thicker than the sensor to minimize lead resistance and the effecgt of the lead resistance changing with temperature.

A.2 Experimental Setup

Prior to the use of the surface-mounted hot-film sensors in the linear cascade, the overall methodology to use the hot-films with a CTA was developed in a small developmental wind tunnel using the well documented unsteady shedding characteristics from a cylinder as a validation flow. The wind tunnel used for this validation is an Aerolab Educational Wind-Tunnel. The tunnel is open-loop, driven by a 7.5 kW motor that can produce test section flow speeds up to 65m/s (213ft/s). The inlet is a bellmouth with a 9.5:1 contraction ratio and a honeycomb flow straightener. The test section is 30.5cm x 30.5cm x 70cm (12in. x 12in. x 24in.) with optical access and several slots in the top for accessibility.

A removable flat plate and a circular copper cylinder were fixed 15.24cm (6in.) above the bottom of the tunnel. The cylinder was painted black and had a diameter (*d*) of 1.6cm (0.63in.). The removable flat plate had an 8:1 elliptical leading edge (curve length to half plate thickness) and was a total of 10*d* in length (*L*). The center of the cylinder and the elliptical leading edge were aligned. The elliptical leading edge was 4*d* downstream of the cylinder. A surface-mounted hot-

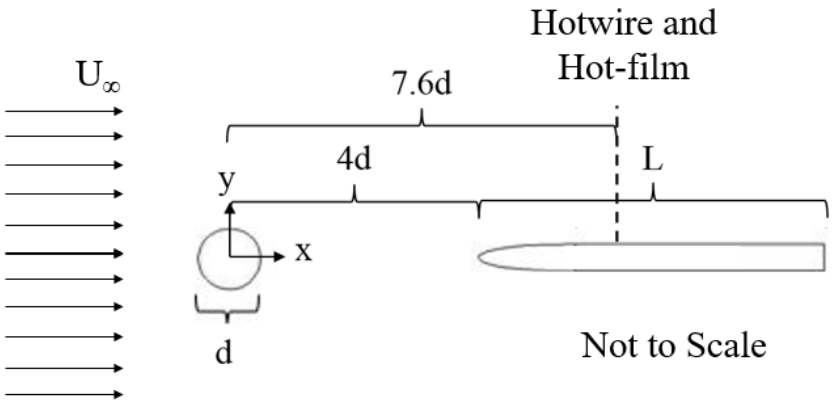

Figure A-2. Schematic of cylinder and flat plate.

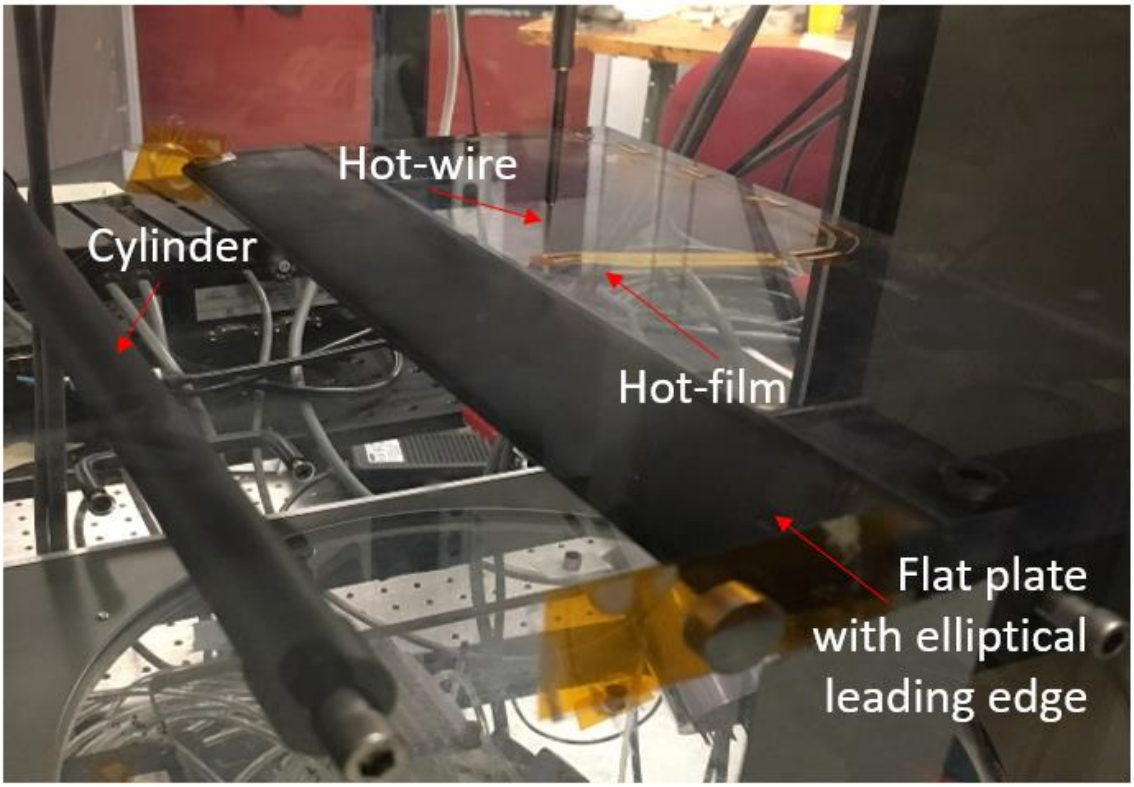

Figure A-3. Picture of cylinder and flat-plate set-up.

film was adhered to the flat plate 7.6*d* downstream from the center of the cylinder. A two-axis traverse system allowed for a hotwire to be positioned 3.7mm (0.147in.) above the flat plate and directly above the hot-film. For each measurement, the two sensors were always positioned in the same downstream plane. The experimental setup is shown in Figure A-2 and Figure A-3.

Hot-film and hotwire measurements were typically sampled at 8 kHz with a 2 kHz low-pass filter on the CTA system. The reference freestream velocity was measured using a Pitot-static probe located 3.5*d* upstream of the cylinder which was removed prior to hot-film and hotwire data acquisition.

Measurements were made over eight Reynolds numbers (Re_d), ranging from 5k to 13k, with the Reynolds number based on the cylinder diameter. At these conditions, the Strouhal number of a cylinder wake can be estimated using the equation provided in Roshko (1953),

$$St = 0.212\left(1 - \frac{12.7}{Re_d}\right). \qquad (A.1)$$

However, Equation A.1 does not take into account the presence of the flat plate, which Roshko found reduced the Strouhal number (1954).

The experimental Strouhal number is calculated using

$$St = \frac{fd}{U_\infty}, \qquad (A.2)$$

where f is the shedding frequency of wake of the cylinder, d is the cylinder diameter, and U_∞ is the freestream velocity. The shedding frequency can be obtained by performing an FFT on the hotwire and hot-film signals.

A.3 Results

Prior to testing the hot-film, baseline measurements downstream of the cylinder were made with the flat plate removed from the tunnel. Figure A-5 depicts an example of the FFT of the signal measured by hotwire 7.6d downstream of the cylinder. The frequency at which the strong narrowband peak in each condition was used to calculate the Strouhal number. The hotwire was traversed across the y-direction (vertically) across the wake of the cylinder with the tunnel set at a Reynolds number of 7409. The Strouhal number was found to be consistent across the wake and close to the expected value calculated using Equation A.1, which was 0.212. These results are summarized in Figure A-4. Hotwire positions very close to y/d = 0, or directly behind the cylinder,

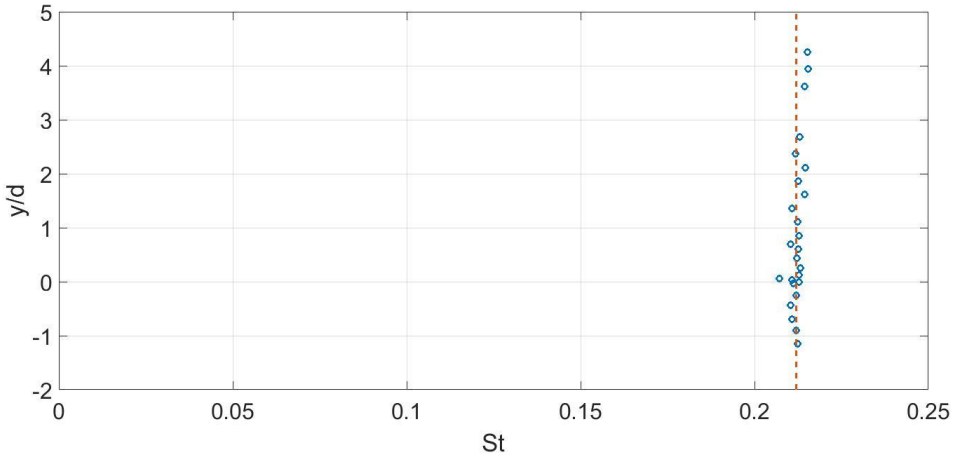

Figure A-4. Strouhal number at various hotwire locations without the flat plate, Re_d = 7409.

show more variations in the Strouhal number than the positions just beyond $y/d = 0$. From the centerline to $y/d \approx 1.5$ is the region with the most data points near the expected value. The positions of the hotwire and hot-film with the flat plate installed are within the region where the Strouhal number is the most consistent and closely agrees with values presented by Roshko (1953, 1954) and Lienhard (1966). A study to insure consistency at various freestream velocities was pursued; therefore, the hotwire was positioned, still without the flat plate, where it would be positioned if the flat plate were present, 7.6*d* downstream and 0.63*d* above the centerline of the cylinder, Figure A-2. Three consecutive data sets of 60s at eight Reynolds numbers were acquired. The Strouhal number at these Reynolds numbers was found to follow the trend of Equation A.1. The decrease in Strouhal number at higher Reynolds numbers reflects results found by Lienhard (1966). These preliminary results lead to the conclusion that the experimental setup and data acquisition process suitably encapsulate the vortex sheet of the cylinder. Therefore the set-up can be used to test the effectiveness and reliability of a hot-film sensor when compared to an adjacent hotwire.

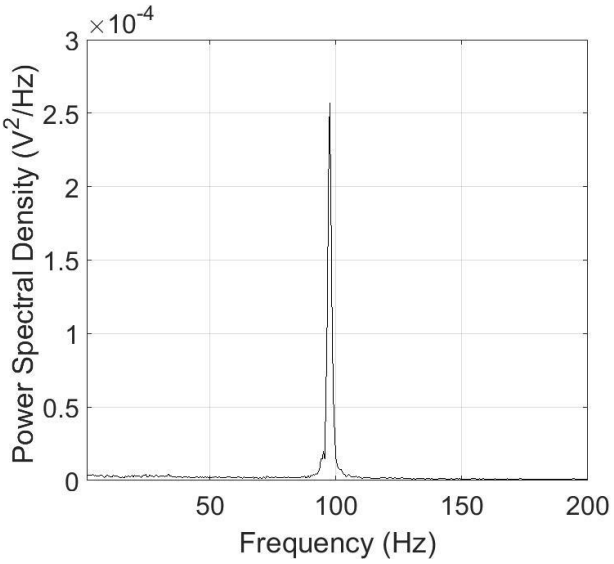

Figure A-5. Example of the frequency spectra without the flat plate.

With the flat plate installed in the tunnel and a hotwire situated directly above the hot-film, it was expected the two sensors should measure similar frequency spectra. At each of eight freestream velocities, five data sets 10s in length were acquired and averaged. Figure A-6 shows the distribution of power versus frequency. The two peaks seen in Figure A-6 are not at the same frequency, which is a consequence of slight variations the freestream velocity, as the data from

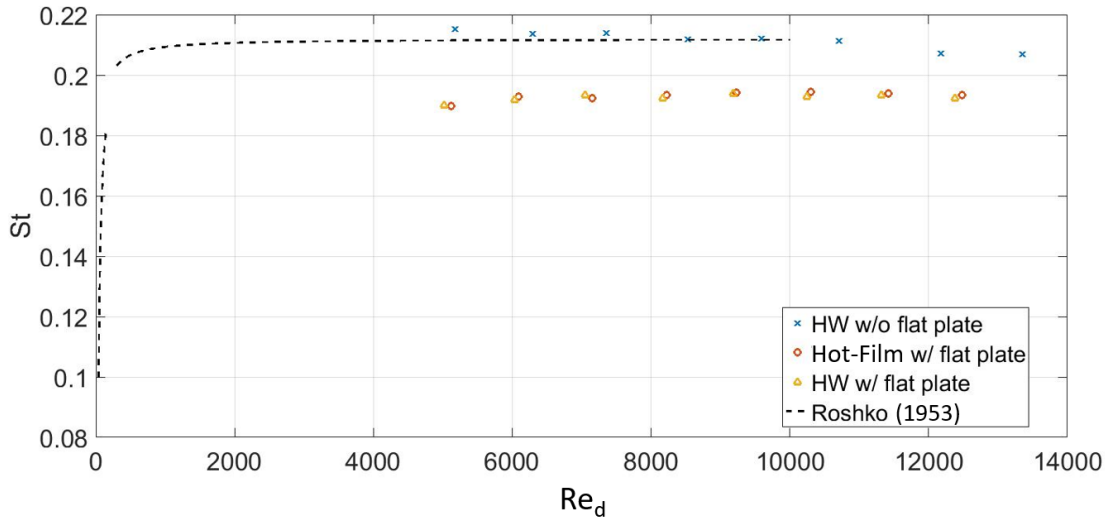

Figure A-7. Comparison of Strouhal number with the hot-film and the hotwire with and without the flat plate.

both sensors could not be obtained simultaneously. However, the signals were similar enough to conclude the hot-film sensor was able to accurately capture the flow, although the magnitude of its power spectral density was considerably less.

The results of the hot-film and hotwire at various Reynolds numbers is summarized in Figure A-7. These non-dimensionalized results show the hot-film and hotwire values are very similar. The greatest difference caused by the variations in freestream velocities at the

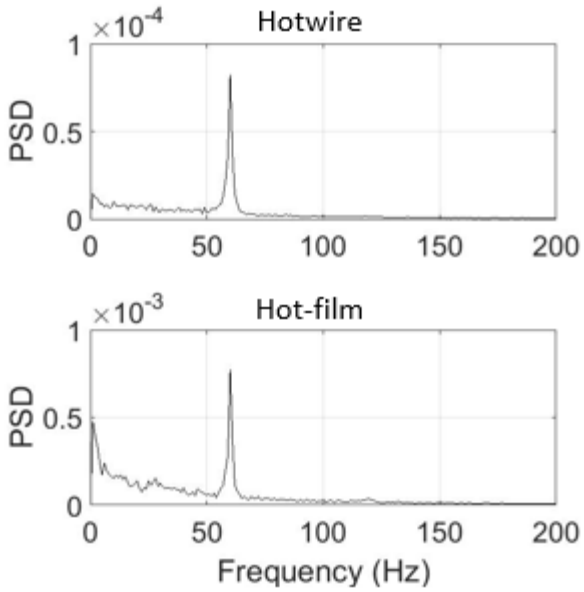

Figure A-6. FFT with power spectral density comparison between the hotwire (top) and the hot-film (bottom), Re_d = 7053.3.

different measurement times. The average Strouhal number decreased with the addition of the flat plate in the cylinder wake, as was expected since Roshko found the same occurrence on the effect of a short plate inserted downstream of a cylinder (1954). Based on these results, it can be concluded that the methodology developed to use the surface-mounted hot-film sensors in a constant temperature mode can be used to accurately measure unsteady flow fluctuations.

A.4 Conclusion

The ability of surface-mounted hot-film sensors to measure the fluctuations in the flow field was verified by characterizing the shedding frequency of a cylinder. A hot-film sensor and an adjacent hotwire located downstream of the cylinder allowed for a direct comparison of the hot film sensor with an established intrusive measurement technique. Experiments were run at several Reynolds numbers, all of which produced Strouhal numbers that were comparable to values found in literature for wake interference of a splitter plate. From these results, it was determined that the surface-mounted hot-film sensor could be used to measure flow unsteadiness thereby obtaining comparable results to those of a hotwire, only non-obtrusively.

B. Single Hot-Film Measurements

B.1 Introduction

Once the ability to use hot-film sensors was developed under the cylinder and flat plate flow describe in Appendix A. The next inquiry was to whether the hot-film would continue to behave similarly to a hotwire in the more complex flow of a turbine endwall.

B.2 Methodology

In the single hot-film sensor configuration, a single sensor and an adjacent hotwire anemometer were moved around the passage. This allowed verification of the hot-film signal within various parts of the flow. The experiments were conducted under flow condition A as described in Table 2-2.

Measurements using a hotwire and a surface-mounted hot-film were acquired in Planes EW3, EW4, and EW5 at x'/C_x of -1.6, -1.13 and -0.69 respectively, as shown in Figure B-1. The plane name nomenclature is based on the arrays described in Section 2.3.1. The hotwire was inserted into the passage from downstream. The probe holder was mounted parallel to the wall and the pitchwise position

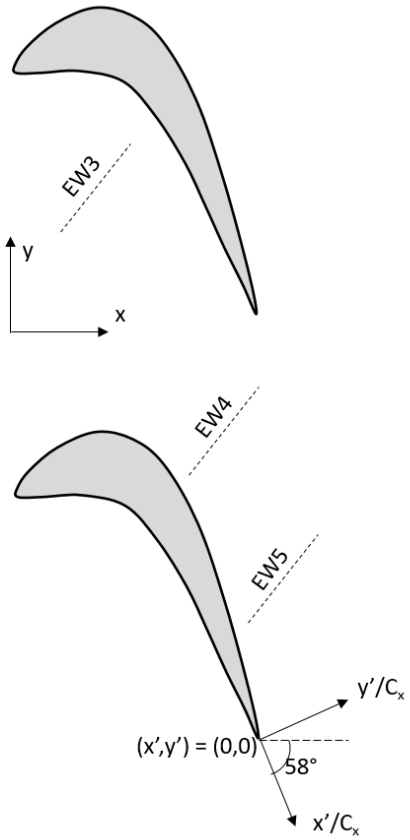

Figure B-1. Single hotwire and hot-film location planes.

was controlled by a low profile National Aperture traverse located downstream of the cascade. The hotwire element was located 0.108C_x above the endwall in the spanwise direction. From PIV, at this height the hotwire moved along the top of the PV, not through the center.

The locations of Planes EW3 and EW5 were determined based on a desire to match the virtual probes in the numerical simulation [Gross 2017]. The location of the PV is not in precisely the same location in the experimental apparatus as it is in the numerical simulation; consequently, to locate the PV in the planes, a hotwire was traversed pitchwise across the passage in a plane perpendicular to the exit flow angle, α_{ex}. The hotwire was positioned at the exit flow angle. The location of the greatest unsteadiness was considered the average location of the center of the PV, since the hotwire traversed across the top of the PV. The location was compared to that obtained

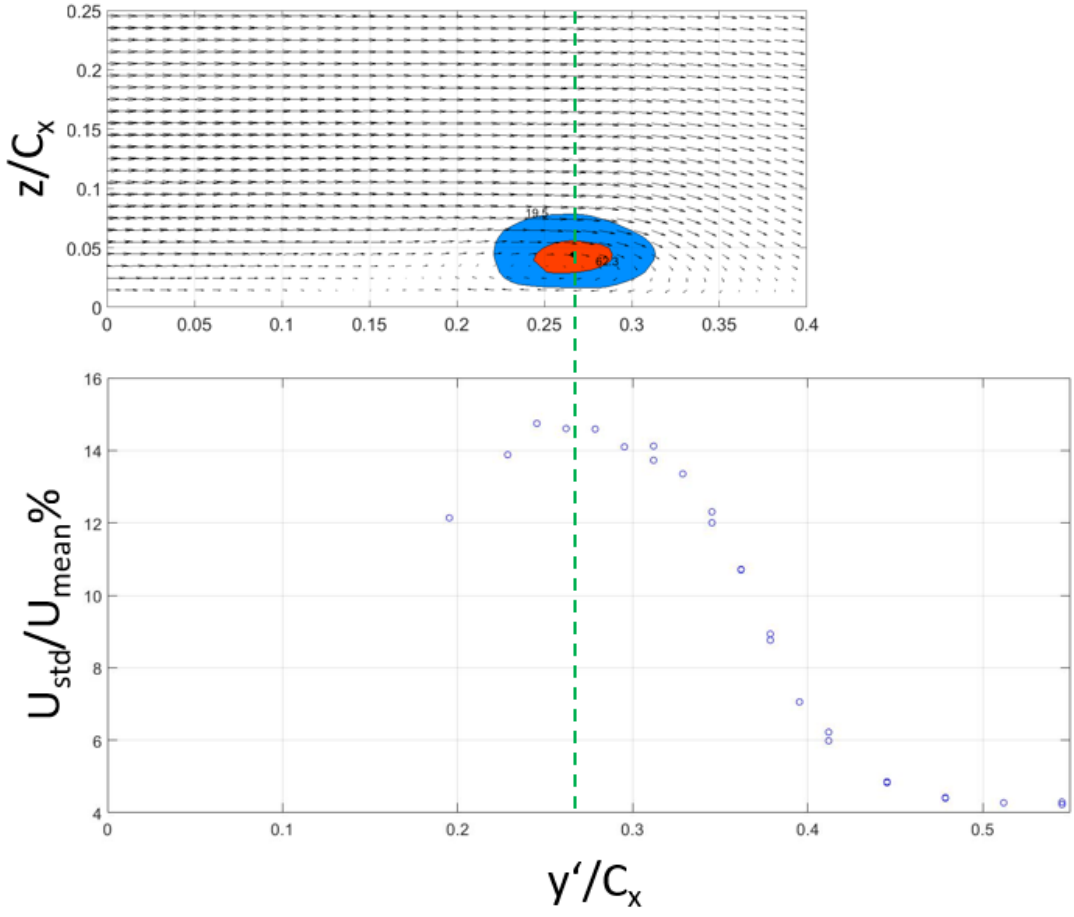

Figure B-2. Top: Velocity vectors and Q-criterion from PIV mid-passage. Bottom: Hotwire unsteadiness measurements across the same plane, z/C_x = 0.08, z/H = 0.02 .

through SPIV for Plane EW3 and Plane EW4, Figure B-2. The unsteadiness of the hotwire velocity, Figure B-2 (bottom), is calculated by dividing the standard deviation of the velocity data by the mean velocity. The PIV data in Figure B-2 (top) shows the time mean velocity vectors and the Q-criterion, thus providing a 2D vortex location. Overall, the two sets of data agreed on the location of the PV for the two planes in which PIV was acquired. Once it was verified that the hotwire unsteadiness reliably provided the location, it was the only method used for locating the PV. The location of the PV was used to position hot-film sensor on the surfaces at the center of the PV in each plane.

A total of four hot-film locations were used. The first three were under the center of the PV in each of the three planes, and the fourth was in Plane EW3 closed to the PS. The hotwire was positioned $0.108C_x$ above the hot-film for every location. In all the PV locations, data was acquired from hot-film with and without the presence of the hotwire above it, allowing an examination of the effects of the hotwire on the flow field.

Numerous sub-records of hotwire and hot-film data were acquired at each measurement location and the frequency spectra from each sub-record was averaged. The resulting frequency spectra are typically the averages of 12 sub-records.

B.3 Results

This set of experiments compared the signal of a surface-mounted hot-film to that of a hotwire placed a small distance above it. This was done to verify that the two sensors obtain comparable results in a more complex flow than that of a cylinder wake, which was investigated in an earlier experiment discussed in Appendix A. The hot-film was placed in four locations throughout the passage: in the PV in Planes EW3, EW4, and EW5, and near the pressure surface in Plane EW3, see Figure B-1. The hot-film signal and the hotwire signal were compared, then the hot-film signal was analyzed with and without the hotwire present in the passage.

The hot-film sensor was placed on the wall directly below the mean center of the PV as determined by the peak unsteadiness previously measured by the hotwire. The hotwire was positioned $0.108C_x$ directly above the hot-film. Figure B-2 compares the hotwire unsteadiness measurements and the Q-criterion derived from SPIV for locating the PV in Plane EW4. It is known that the frequency spectrum is sensitive to the position of the sensor relative to the vortex, which makes controlling the difference in position between the sensors imperative. For all sensor locations, flow condition A from Table 2-2 was studied. The raw data from both the hotwire and the hot-film sensor were processed through a Fast Fourier Transform (FFT) to calculate the power spectral density (PSD). Figure B-4 shows the difference in magnitude between the data

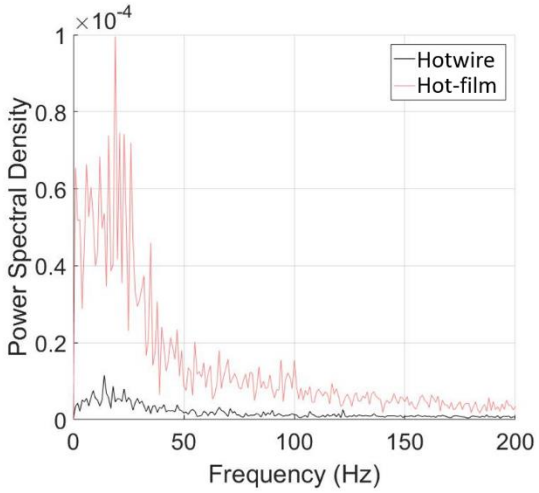

Figure B-4. The magnitude of the power spectral density of the hot-film is much greater than that of the hotwire.

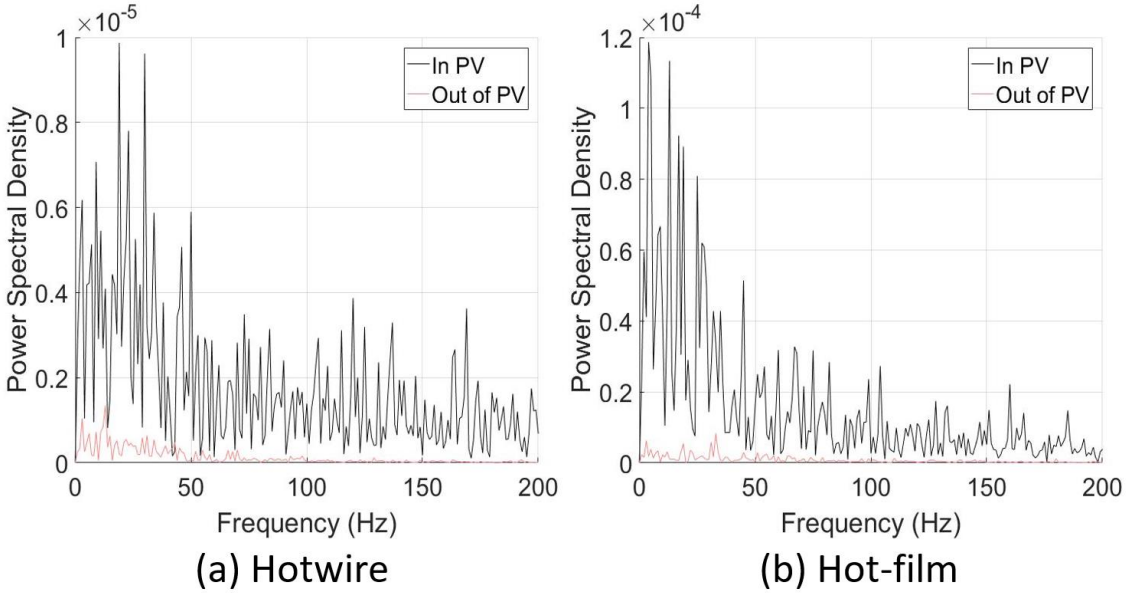

Figure B-3. Comparison of fluctuations in and out of the PV using (a) a hotwire and (b) a hot-film.

collected from the hot-film sensor as compared to the hotwire, caused by a significant difference in the operating resistance between the two types of sensors.

Along with the hot-film and the hotwire adjacent to the PV in Plane EW3, the hot-film and hotwire were positioned outside the region of the PV near the pressure side of the passage. This allowed for verification that the sensors were picking up real flow phenomena as opposed to noise. Figure B-3 shows the increase in the turbulence when the sensors were adjacent to the PV and the presence of a narrow band of energetic frequencies; whereas, outside the PV region, the unsteady energy content was much lower. Although the effects of the PV are not apparent in the pressure side region, turbulence is still present, which was expected under the high FSTI of flow condition A. The effects of the difference in distance between the hotwire and the surface-mounted thin-film is clearly seen when the sensors are in the PV, but location also has some effects toward the pressure side.

Once it was verified that the hotwire and hot-film were in the PV, the sensor was relocated and positioned adjacent to the PV measurements in the three planes discussed. Figure B-5 compares the hotwire and hot-film measurements at each plane. The two sensors in Plane EW3 show similar FFTs, where the energy is highest between 10Hz and 40Hz, with a peak around 25Hz. In Plane EW4, the energy is still concentrated below 50Hz, although the hotwire picked up a strong peak around 40Hz that appears much weaker for the hot-film. The hotwire spectrum has two peaks,

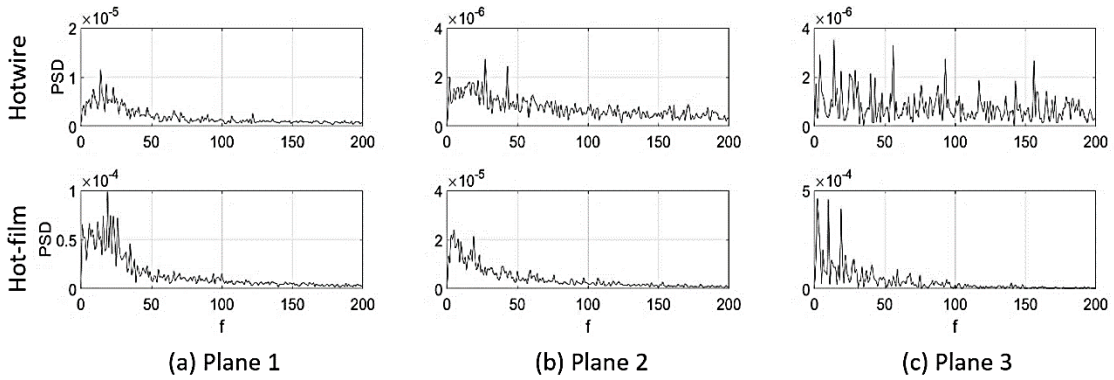

Figure B-5. Comparison of Hotwire (top) and Hot-film Power Spectral Density along the passage vortex in (a) Plane EW3, (b) Plane EW4, and (c) Plane EW5.

~25Hz and ~40Hz, which are shifted to slightly higher frequencies compared to the peaks shown in the adjacent hot-film. In Plane EW5 the hotwire spectrum is broader with several peaks, whereas the hot-film shows a concentration of energy below 100Hz. In Plane EW5, the significant variations in the spectra between the two sensors are likely due to the hotwire being mounted a distance $0.108C_x$ above the surface. The PV interacts with the strong corner separation in the Plane EW5 region. The frequency spectrum is expected to be very sensitive to the location of the sensor in the flow in that area.

The measured frequencies were non-dimensionalized as defined in Equation 3.2 to compare directly with spectra from the ILES simulation. The locations of Probes 3 and 4 from the initial numerical simulation [Gross et al. 2017] correspond to the location of the PV in Planes EW3 and EW5 respectively. Since the probes in the numerical simulation were offset above the endwall, the hotwire data shown in Figure B-6 were expected to provide a better comparison than the surface-mounted hot-films. The general shape of the spectra is similar between the simulation and experiment, Figure 3-4 and Figure B-6. The energy content of Probe 3 is greatest when $f^* < 0.75$

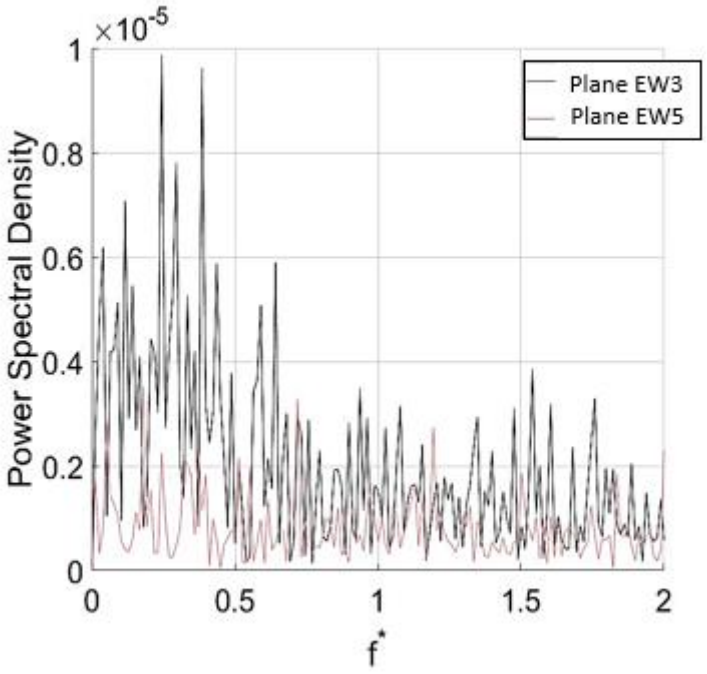

Figure B-6. PSD plot of hotwire data in the passage vortex.

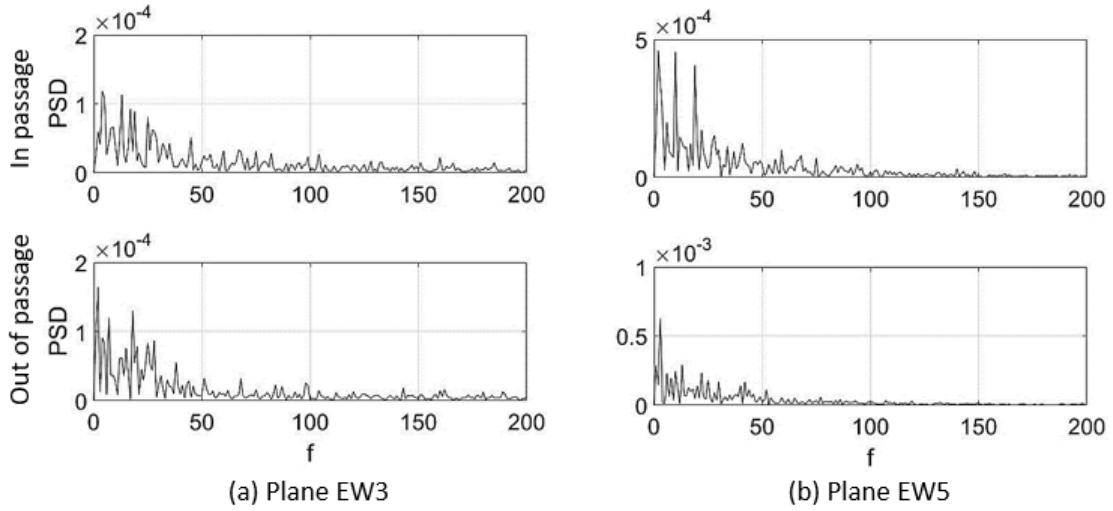

Figure B-7. Hot-film frequency spectra change when the hotwire is present in (top) and absent from (bottom) the passage as shown in the PV in Plane EW3 (left) and Plane EW5 (right).

with a broadband peak at $f^* \approx 0.35$. At Probe 4, the energy is strongest when $f^* < 0.5$. There are additional peaks beyond $f^* = 0.5$ in both the simulation and experiment.

The purpose of the hot-film sensors is to provide a non-intrusive measurement technique. Inserting the hotwire into the passage was expected to have a blockage effect on the flow field. When the hot-film sensor was operated without the hotwire in the test section, the frequencies at which the peaks occurred shifted in an unpredictable manner, as shown in Figure B-7. For Plane EW5, the peaks shifted to slightly higher frequencies with the removal of the hotwire; the peaks in Plane EW3 shifted to lower frequencies.

B.4 Conclusions

For the investigation with a single hot-film compared to a hotwire under the high FSTI flow condition, the sensors were positioned in the L2F blade passage in three planes at the mean center of the PV, as determined by an unsteadiness trace completed with the hotwire. The two sensor types showed minor differences in results, caused by the difference in location, the hot-film being mounted on the surface and the hotwire being above the surface. The hotwire and hot-film both showed a broad band in the low frequency range, matching the ILES results and indicating that the flow is turbulent. The hotwire provided comparable results to the numerical simulation, as

the probes where similarly situated off the endwall. Both experimental sensor types reinforced the dimensional frequency of the bimodal behavior of the PV at a Reynolds number of 100k.

The hot-film did show a noticeable and unpredictable shift in the measured frequencies with removal of the hotwire from the flow. This indicated that the presence of the hotwire does indeed influence the flow field. Therefore, the non-obtrusive hot-film sensor provides the benefit of not creating new flow structures in the flow field of interest.

C. Hot-Film Location Tables

Two coordinate systems were used to locate the sensors within a passage. The first was used the axial direction as the x-component. The origin of this system aligns with the trailing edge of the pressure side blade projected up to where it intersects the leading edge. The second coordinate system uses exit flow angle as the x-component. The origin is located on the trailing edge of suction side blade. Figure C-1 shows the origins of the two coordinate systems.

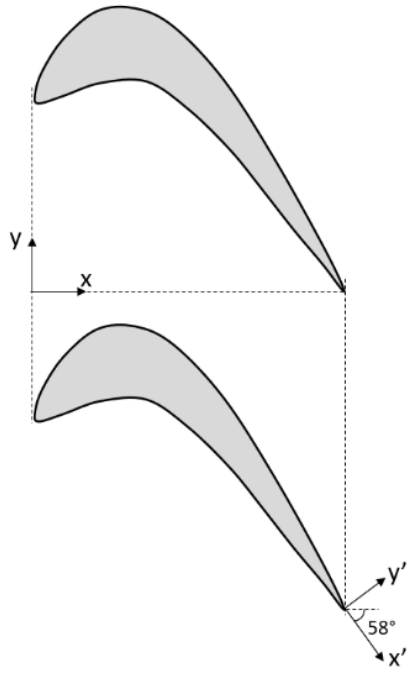

Figure C-1. Location of origins for the two coordinate systems.

C.1 Simultaneous Hot-Film Sensors

Table 3. Position of a sensor in each array.

Sensor	x/C_x	y/C_x	x'/C_x	y'/C_x
EW1a	-1.0	0.17	-2.23	-0.93
EW2a	-0.03	0.63	-2.13	-0.07
EW2b	-0.06	0.61	-2.13	0.10
EW2c	-0.08	0.59	-2.13	0.14
EW3a	0.40	0.17	-1.18	0.24
EW3b	0.38	0.20	-1.22	0.20
EW3c	0.36	0.06	-1.25	0.24
EW4a	0.59	-0.18	-1.11	0.22
EW4b	0.62	-0.17	-1.11	0.25
EW4c	0.65	-0.15	-1.11	0.29
EW4d	0.68	-0.13	-1.11	0.32
EW4e	0.71	-0.11	-1.11	0.50
EW5a	0.77	-0.57	-0.70	0.16
EW5b	0.79	-0.55	-0.70	0.19
EW5c	0.82	-0.53	-0.70	0.22
EW5d	0.85	-0.51	-0.70	0.26

Table 4. Suction surface hot-film locations

Sensor	x	z	x/Cx	z/H
SS1	1.80	4.15	0.30	0.16
SS2	3.15	4.15	0.52	0.16
SS3	3.38	1.77	0.57	0.07
SS4	4.70	4.15	0.783	0.16
SS5	5.10	0.76	0.85	0.03
SS6	5.10	1.77	0.85	0.07

C.2 Concurrent Hot-Film and Flow-Visualization

Table 5. Hot-film sensor locations during concurrent measurements of PIV and flow-visualization.

Sensor	x/C_x	y/C_x	x'/C_x	y'/C_x
EW4a	0.58	-0.29	-1.03	0.15
EW4b	0.62	-0.27	-1.03	0.19
EW4c	0.64	-0.25	-1.03	0.22
EW4d	0.67	-0.24	-1.03	0.25
EW4e	0.70	-0.22	-1.03	0.29
EW4f	0.73	-0.20	-1.03	0.32
EW4g	0.76	-0.18	-1.03	0.36
EW4h	0.78	-0.17	-1.03	0.39

References

Bear, P. S., “On the Experimental Evaluation of Loss Production and Reduction in a Highly Loaded Low Pressure Turbine Cascade,” Masters Thesis, Wright State University, 2016

Bellhouse, B., and Schultz, D., “Determination of Mean and Dynamic Skin Friction, Separation and Transition in Low-Speed Flow with a Thin-Film Heated Element,” *J. of Fluid Mechanics*, Vol. 24, No 2, pp. 379-400, 1966, doi: 10.1017/50022112066000715

Benton, S. I., Bons, J. P., and Sondergaard, R., “Secondary Flow Loss Reduction through Blowing for a High-Lift Front-Loaded Low Pressure Turbine Cascade,” *J. of Turbomachinery*. Vol. 135, No. 2, pp. 021020-1-8, 2012, doi: 10.1115/1.4007531

Bruun, H. H. (1995) *Hot-Wire Anemometry Principles and Signal Analysis*. Oxford University Press Inc., New York

Clark, J. P., Koch, P. J., Puterbaugh, S. L. Schmitz, J. T., Morris, S. C., Ma, R., and Corke, T. C. (2010) “Highly Loaded Low-Pressure Turbine: Design, Numerical and Experimental Analysis,” AFRL Report: AFRL-RZ-WP-TP-2010-2143.

Collis, D. C., and Williams, M. J., “Two-Dimensional Convection from Heated Wires at Low Reynolds Numbers,” *J. of Fluid Mechanics*. Vol. 6, No. 3, pp. 357-384, 1959, doi: 10.1017/50022112059000696

Denton, J. D., "Loss Mechanics in Turbomachines," *J. of Turbomachinery*. Vol. 115, No. 4, pp. 621-656, 1993, doi: 10.115/1.2929299

Devenport, W. J., and Simpson, R. L., "Time-Dependent and Time-Averaged Turbulence Structure near the Nose of a Wing-Body Junction," *J. of Fluid Mechanics*. Vol. 210, pp. 23-55, 1990, doi: 10.1017/50022112090001215

Dickel, J., Marks, C. R., Clark, L., Sondergaard, R., and Wolff, M., "Non-Axisymmetric Endwall Contouring of Front-Loaded High-Lift Low Pressure Turbines," 2018 AIAA Aerospace Sciences Meeting, 8-12 January 2018, doi: 10.2514/6.2018-2125

George, W. K., Beuther, P. D., and Shabbir, A., "Polynomial Calibration for Hot Wires in Thermally Varying Flows," *Experimental Thermal and Fluid Science*. Vol. 2, No. 2, pp. 230-235, 1989, doi: 10.1016/0894-1777(89)90038-1

Gross, A., Romero, S., Marks, C., and Sondergaard, R., "Numerical Investigation of Low-Pressure Turbine Endwall Flows," 54th AIAA Aerospace Sciences Meeting, 4-8 January 2016, doi: 10.2514/6.2016-0331

Gross, A., Marks, C. R., and Sondergaard, R., "Numerical Investigation of Low-Pressure Turbine Junction Flow," *AIAA Journal*. Vol. 55, No. 10, pp. 3617-3621, 2017 , doi: 10.2514/1.J055859

Harrison, S., "Secondary Loss Generation in a Linear Cascade of High-Turning Turbine Blades," *J. of Turbomachinery.* Vol. 112, No. 4, pp. 625-632, 1990, doi: 10.1115/1.2927703

Heron, I., and Myose, R. Y., "Delta Wing Vortex-Burst Behavior Under a Dynamic Freestream," *J. of Aircraft*, Vol. 46, No. 5, pp. 1500-1512, 2009, doi: 10.2514/1.36697

Hodson, H., "Boundary Layer and Loss Measurements on the Rotor of an Axial-Flow Turbine," *J. of Engineering for Gas Turbines and Power*, Vol. 106, No. 2, 1984, doi: 10.1115/1.3239577

Hunter, Kevin, (2017) "Ensuring Operationally-Ready Energy," Naval Power and Force Projection, Summer 2017, pg. 26.

IFA 300 Constant Temperature Anemometer System Instruction Manual, TSI Incorporated, 2010, Shoreview, MN.

King, L. S., "On the Convection Heat Transfer from Small Cylinders in a Stream of Fluid: Determination of the Convection Constants of Small Platinum Wires with Applications to Hot-Wire Anemometry," *Phil. Trans. Roy. Soc. London*, 214A, 373-432, 1914

Kline, S. J., Reynolds, W. C., Schraub, F. A., and Runstadler, P. W., "The Structure of Turbulent Boundary Layers," *J. of Fluid Mechanics.* Vol. 30, No. 4, pp. 741-773, 1967, doi: 10.1017/50022112067001740

Kramers, H., "Heat Transfer from Spheres to Flowing Media," *Physica*, Vol 12, No 2-3, 1946

Lambourne, N. C., and Bryer, D. W., "The Bursting of Leading-Edge Vortices – Some Observations and Discussion of the Phenomenon," *ARC R & M* 3282, April 1961

Lange, E. A., Elahi, S. S., and Lynch, S. P., "Time-resolved PIV Measurements of the Effects of Freestream Turbulence on Horseshoe Vortex Dynamics," 2018 AIAA Aerospace Sciences Meeting, 8-12 January 2018, doi: 10.251416.2018-0358

Langston, L. S., Nice, M. L., and Hooper, R. M., "Three-Dimensional Flow Within a Turbine Cascade Passage," *J. of Engineering for Power*. Vol. 99, No. 1, pp. 21-28, 1977, doi: 10.1115/1.3446247

Langston, L. S., (2001), "Secondary Flows in Axial Turbines – A Review," Annals of the New York Academy of Sciences, 934: 11-26. doi: 10.1111/j1749-6632.2001.tb05839.x

Lienhard, J. H., "Synopsis of lift, drag, and vortex shedding frequency data for rigid circular cylinders," *Washington State University College of Engineering – Research Division Bulletin*, 1966, pp. 32

Marks, C. R., "Surface Stress Sensors for Closed Loop Low Reynolds Number Separation Control," Ph.D. Dissertation, Wright State University, 2011

Marks, C., Sondergaard, R., Bear, P., and Wolff, M., "Reynolds Number Effects on the Secondary Flow of Profile Contoured Low Pressure Turbines," 54th AIAA Aerospace Sciences Meeting, 4-8 January 2016, doi: 10.2514/6.2016-0114

McQuilling, M. W., "Design and Validation of a High-Lift Low-Pressure Turbine Blade," Ph.D. Dissertation, Wright State University, 2007.

Nakayama, A., Stack, J. P., Lin, J. C., and Valarezo, W. O., "Surface Hot-Film Technique for Measurements of Transition, Separation, and Reattachment Points," 24th AIAA Fluid Dynamics Conference, 6-9 July 1993, Orlando, Florida, doi: 10.2514/6.1993-2918

Praisner, T. J., and Smith, C. R., "The Dynamics of the Horseshoe Vortex and Associated Endwall Heat Transfer – Part I: Temporal Behavior," *J. of Turbomachinery*, Vol. 128, No. 4, 2006, pp. 747-754. Doi: 10.1115/1.2185676

Roshko, A., (1953) "On the Development of Turbulent Wakes from Vortex Streets," National Advisory Committee for Aeronautics 1953, Washington, D.C.

Roshko, A., (1954) "On the drag and shedding frequency of two-dimensional bluff bodies," 01 July 1954, National Advisory Committee for Aeronautics; Washington, DC, United States

Sabatino, D. R., and Smith, C. R., "Boundary Layer Influence on the Unsteady Horseshoe Vortex Flow and Surface Heat Transfer," *J. of Turbomachinery*. Vol. 131, No. 1, pp. 011015-8, 2009, doi: 10.1115/1.2813001

Sieverding, C. H., "Recent Progress in the Understanding of Basic Aspects of Secondary Flows in Turbine Blade Passages," *J. of Engineering for Gas Turbines and Power*. Vol. 107, No. 2, pp. 258-264, 1985, doi: 10.1115/1.3239705

Soltani, M. R., and Bragg, M. B., "Early Vortex Burst on a Delta Wing in Pitch," *AIAA Journal*, Vol. 31, No. 12, pp. 2283-2289, 1993, doi: 10.2514/3.11926

Stack, J. P., Mangalam, S. M., and Berry, S. A., "A Unique Measurement Technique to Study Laminar-Separation Bubble Characteristics on an Airfoil," 19th AIAA Fluid Dynamocs, Plasma Dynamics, and Laser Conference, 1987, doi: 10.2514/6.1987-1271

Veley, E., Marks, C., Anthony, R., Sondergaard, R., Fletcher, N., and Wolff, M., "Unsteady Flow Measurements in a Low Pressure Turbine Passage using Surface Mounted Thin Film Sensors," 53rd AIAA/SAE/ASEE Joint Propulsion Conference, 2017, July 10th-12th, Atlanta, GA. Doi: 10.2514/6.2017-4825

Veley, E. M., Marks, C. R., Anthony, R., Sondergaard, R., and Wolff, M., "Unsteady Flow Measurements in a Front Loaded Low Pressure Turbine Passage," AIAA SciTech 2018-2124, 8-12 January 2018, doi: 10.2514/6.2018-2124

Vera, M., de la Rosa Blanco, E., Hodson, H., and Vazquez, R., "Endwall Boundary Layer Development in an Engine Representative Four-Stage Low Pressure Turbine Rig," *J. of Turbomachinery*. Vol. 131, No.1, pp. 011017-9, 2009, DOI:10.1115/1.2952382

Wang, H. P., Olson, S. J., Goldstein, R. J., and Eckert, E. R. G., "Flow Visualization in a Linear Turbine Cascade of High Performance Turbine Blades," *J. of Turbomachinery*. Vol. 119, No. 1, pp. 1-8, 1997, doi: 10.1115/1.2841006

White, F. M. (1999) *Fluid Mechanics* 4th Ed. WCB/McGraw-Hill, Boston

Zhang, Z. F., Mahallati, A., and Sjolander, S. A., "Hot-Film Measurements of Boundary Layer Transition, Separation and Reattachment on a Low-Pressure Turbine Airfoil at Low Reynolds

Numbers," 38th AIAA/ASME/SAE/ASEE Joint Propulsion Conference, 7-10 July 2002, Indianapolis, Indiana. Doi: 10.2514/6.2002-3643